This is to certify that the
thesis entitled

RARE EARTH ELEMENT MOVEMENT DURING INCIPIENT ALTERATION OF PYROXENES IN GUATEMALAN CORESTONES

presented by

ANGELA ROSE DONATELLE

has been accepted towards fulfillment
of the requirements for the

M.S. degree in GEOLOGICAL SCIENCES

Michael Anthony Velbel
Major Professor's Signature

1 Aug 2008
Date

RARE EARTH ELEMENT MOVEMENT DURING INCIPIENT ALTERATION OF PYROXENES IN GUATEMALAN CORESTONES

By

Angela Rose Donatelle

A THESIS

Submitted to
Michigan State University
In partial fulfillment of the requirements
for the degree of

MASTER OF SCIENCE

Geological Sciences

2008

ABSTRACT

RARE EARTH ELEMENT MOVEMENT DURING INCIPIENT ALTERATION OF PYROXENES IN GUATEMALAN CORESTONES

By

Angela Rose Donatelle

This study investigates the role of pyroxenes in the redistribution of rare earth elements (REE) in whole-rock geochemical data previously reported for a weathered corestone system in SE Guatemala. Previous work on spheroidal weathering has shown that variations in REE abundances can accompany minor changes in major elements.

Weathered augites within the corestone-interior are enriched in light REE (LREE), with abundances above fresh rock values. Several augites from the more weathered corestone-rind have passed the onset of weathering and have LREE similar to fresh rock values without a negative Ce anomaly. Products found within the augite dissolution features host the LREE during initial weathering. As alteration continues the products are subsequently depleted in LREE and lose the negative Ce anomaly. Identical behavior has been reported from intermediate degrees of weathering in whole-rock studies of spheroidal weathering.

Augite alteration creates an environment suitable for precipitation of LREE rich products, but the LREE abundances and patterns of the products are sufficiently unlike those of the primary augite that the augite itself is not the main source of the LREE in augite's weathering products. The source of the LREE must therefore be a phase other than augite, such as glass or microcrystalline groundmass. Formation of LREE rich secondary phases is associated with increased LREE and Ce anomaly in the whole-rock REE signature of the core and rind of the system.

To Tom Hickson and Lisa Lamb. Two amazing teachers, without whom I would never have known the significance and beauty of science, or believed that I could become a geologist.

ACKNOWLEDGEMENTS

I want to give a heartfelt thank you to Michael Velbel who was kind enough to take me on as a student when I got to MSU and has been the best advisor I could have hoped for. My committee; Lina Patino for requiring me to explain my research in two sentences and Tom Vogel for sitting on my committee even after his retirement. Ewa Danielewicz for her help and great conversations during SEM sessions. Karl Henderson at the UofM for his help on the microprobe.

This project was supported by NASA Mars Fundamental Research Program grant NNG05GL77G (M. Velbel, Principal Investigator).

Thank you to all my family and friends. My Mom, Dad, Anne, Dave, Hannah Steven, Anna, Daniella, and Tony. Thank you to the world's best sister and friend Anne Szymanski and my niece Hannah who were always there to hang out when I needed a study/reality break. To the best brother-in-law I could ever ask for Dave whom has been a great support both as a friend and as a fellow colleague. My best friend Stephanie Januszewski for understanding that though I am not in MN anymore, and I don't keep in touch as much as I should, that she is still my closest friend in the entire world and that will never change! Michael "Dutchy" Kramer for earning the title of "the best roommate ever" simply by putting up with me for a year. Paula and Aaron Tarone for being two of the greatest friends I could have asked for in East Lansing. The Advanced Petrology class, especially Paulo Hidalgo, Lance Paquette, Liz Connover, Maisie Nichols, and Ryan Currier for helping me with my petrology and working on homework together, as well as

the crazy times at the Peanut Barrel, usually instigated by Paulo and Ryan. The great geology undergrads at MSU including, Erin Argue and Betsey Woodward. To all my fellow graduate students. Jen Deloge and Bob Alysworth who are always fun to talk to and hang out with at the bar. Thank you to Sarah Kraig for being another fashion forward geologist/biologist (science geek) with me the last two years; there should be more of us in the world. Thank you to my newest friend in the geology department, Ania Losiak. I have enjoyed working with you and I look forward to being your geology sister as we work on our PhD's under the supervision of Velbs. My PCHEM buddy Ryan Vannier who sat through many an entertaining lecture (let's just say "eraser boy" and leave it at that!). To my non geo-savy friends in E.L. including Nick Nevins, Lisa Ramos, and Heather Klienhardt. To my mineralogy students from the past two years. I greatly appreciate your patience as I have improved my teaching skills and getting to hang out once you are no longer my students. Thank you to everyone else that I have come into contact with over my past three years here at MSU. It has been a wonderful experience that I will never forget.

TABLE OF CONTENTS

LIST OF TABLES

LIST OF FIGURES

INTRODUCTION

The purpose of this study is to determine whether the dissolution of pyroxenes contributes LREE to the increased abundance of LREE in corestone samples from weathered regoliths on volcanic rocks in SE Guatemala. The petrographic and geochemical data will also be useful in advancing the community's understanding of incipient weathering of pyroxenes and volcanic rocks.

Weathering is traditionally divided into two types, physical or chemical alteration of a rock or mineral (Taylor and Eggleton, 2001). The former is observed mainly through visible alteration features and changes in volume and other physical properties, and the latter through changes in mineral abundances and/or bulk elemental composition of the weathered material (Taylor and Eggleton, 2001; Price and Velbel, 2003).

Current techniques for analyzing chemical weathering focus on major elements (Price and Velbel, 2003). Several studies have shown that accessory phases containing high abundances of REE preferentially release REE during dissolution (Minarik et al., 1998; Harlavan and Erel, 2002). However, preferential dissolution of REE in major rock-forming phases is hard to identify due to sometime low abundances of REE in these phases. Studies show that anomalous whole-rock REE patterns, in what were presumed to be fresh samples, are sometimes caused by the incipient weathering of the rocks and are not a primary feature (Eggleton et al., 1987; Cotten et al., 1995; Cameron, 1998; Wade, 2002; Patino et al., 2003). The change in REE in samples that show only minor movement of the major elements indicate that REE are mobilized extensively at the same time as some major elements are initially mobilized. REE are therefore an appropriate tool to use in the search for new ways to characterize the onset of alteration, because

large relative changes in trace-element abundances are easier to measure than small relative changes in major element abundances.

Corestones form during spheroidal weathering (Ollier, 1971) of columnar-jointed or fractured (physically weathered) volcanic rocks. They provide a convenient setting in which to observe weathering and study the movement of REE during the different stages of weathering. Patino et al. (2003) examined multiple corestones and associated weathering rinds that show an increase in the abundance of REE (with much smaller increases in Ce) during initial stages weathering (represented within the corestone). Increased weathering (represented by the rinds and shells) subsequently leads to a decrease in REE (with much smaller decreases in Ce) and in some instances the return to fresh rock values or whole-rock values that were below those of the fresh rock. The Ce anomalies that formed during weathering are the result of the immobility of Ce in solution when compared to other REE.

Recent work on whole-rock REE mobility during initial stages of weathering is redefining how we consider and characterize the onset of weathering. Examination of REE host minerals and REE movement during incipient alteration is needed to expand understanding of the onset of weathering beyond the stage measurable by whole-sample major-element chemistry. This study investigates the contribution of pyroxene (the most abundant phenocryst phase with significant concentrations of REE) to REE increases seen within the whole-rock analyses of corestones.

PREVIOUS WORK

Determining the influence of pyroxene weathering on increases in whole-rock REE during early weathering requires an understanding of the pyroxene structure, incorporation of REE into the pyroxenes, and where and how the first stages of pyroxene weathering occur.

REE and Pyroxenes

Pyroxenes consist of alternating chains of Si-tetrahedra and cation-octahedra. The composition of pyroxene is categorized according to the relative proportion of three major-element end-members, defined by the major cations Mg, Fe, and Ca (Figure 1, from Deer et al. (1992)). Cations are site-specific; ions with similar valence and ionic radii have a preference for similar sites. The general pyroxene formula $M2M1T_2O_6$ (Cameron and Papike, 1981; Morimoto et al., 1988; Deer et al., 1992) expresses the location of cations within the octahedral sites (M2 and M1) and the tetrahedral site (T) (Figure 2). The M2 site tends to accommodate large cations, larger than approximately 1Å in size, and the M1 site cations that are less than 1Å (Onuma et al., 1968; McKay, 1989; Deer et al., 1992). The Ca^{2+} ion has a radius of around 1.08Å and is found primarily in the M2 site of the pyroxene structure (Onuma et al., 1968; Cameron and Papike, 1981; McKay, 1989; Deer et al., 1992).

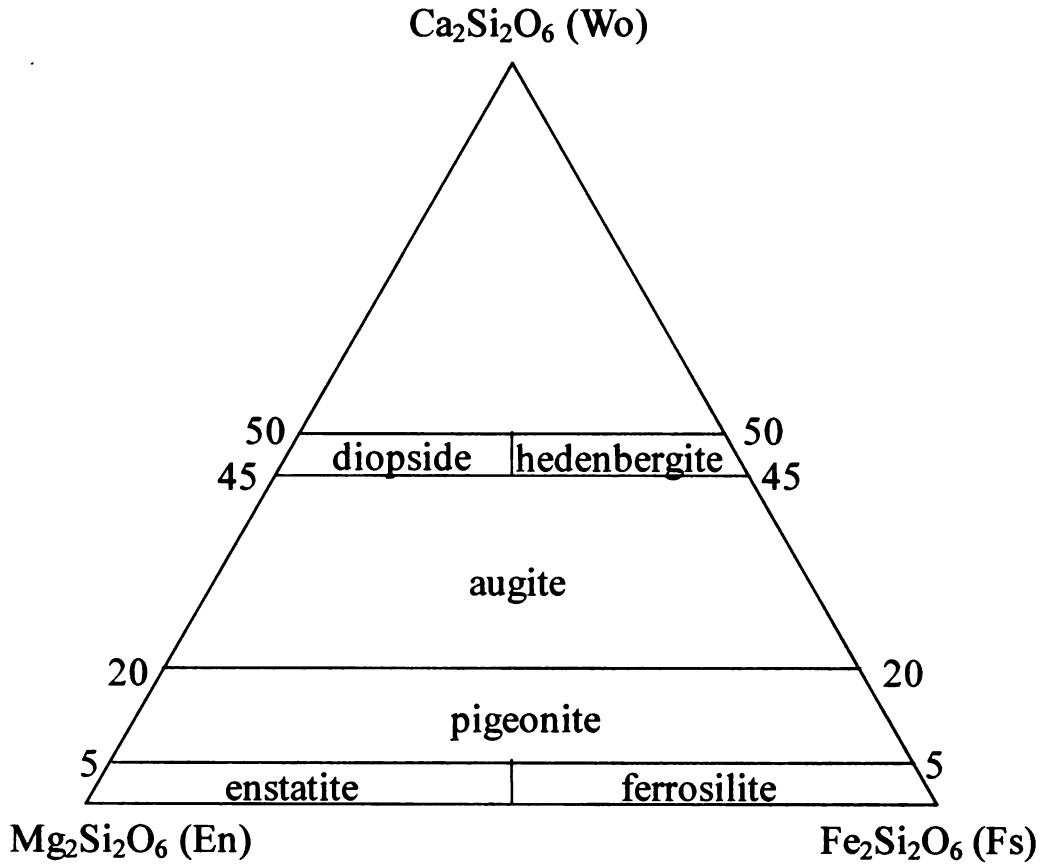

Figure 1. Pyroxene quadrilateral showing the different pyroxene end members. Adapted from Deer et al. (1992).

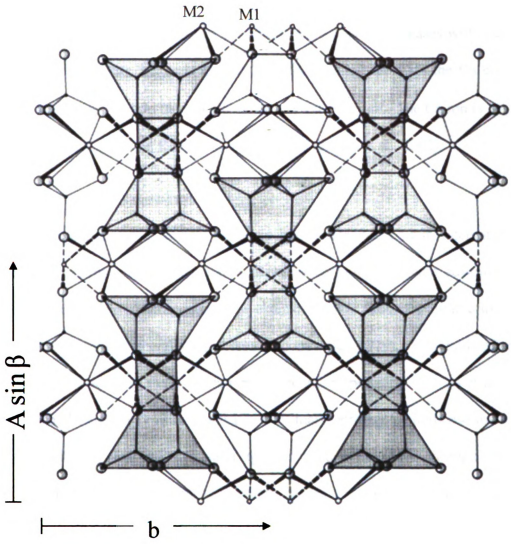

Figure 2. Diagram of the crystal structure of a typical pyroxene (Cameron and Papike, 1981).

The abundance of LREE (light REE) incorporated into the pyroxene structure increases with decreasing ionic radius (James et al., 2002). REE content increases with increasing Ca (McKay et al., 1986; James et al., 2002). This relationship with the Ca content is caused by Ca^{2+} entering into the M2 site of the crystal structure. The Ca ion is large and "props open" space allowing REE to fit in the crystal (James et al., 2002).

Weathering Features

The alteration pattern of a specific phase is highly dependent upon internal mineral structure, but internal crystal-chemical weaknesses can only be taken advantage of if fluids can reach them. Alteration is most extensive when fluid is available to interact with a large amount of mineral surface area (Stoops et al., 1979). The fluids often gain access to mineral surfaces through primary or secondary porosity. Stoops et al. (1979) describe secondary porosity as an extension of primary porosity. Fluids use fractures (a physical weathering feature) and other (primary) voids to move through the rock, corroding minerals and increasing the "empty spaces" or pores, and thus creating the secondary porosity. Stoops et al. (1979) describe three types of pores that occur within rocks. The first is transmineral pores that crosscut the entire rock without following grain boundaries. Intermineral and intramineral pores describe the interaction of fractures with individual grains; the former follow grain boundaries and affect multiple mineral grains and the latter follow fractures and cleavages that cut across individual grains.

Major Elements and Weathering

Weathering of regolith is largely dependent upon rock composition (Nesbitt and Wilson, 1992). The study of weathering and the processes involved has relied on the use of major element weathering indices such as the Chemical Index of Alteration (CIA; Nesbitt and

Young, 1982) to characterize the movement of elements and progression of alteration. These and other indices use major element oxides to calculate a number for the degree of alteration a sample has undergone (Price and Velbel, 2003). CIA (Nesbitt and Young, 1982) is defined as

$$CIA = (100)[Al_2O_3/(Al_2O_3+CaO+Na_2O+K_2O)]$$

As a rock weathers the mobile major elements are removed from their primary host phases and they either leave the system in solution or are re-deposited in a secondary phase (Taylor and Eggleton, 2001). Aluminum is typically immobile compared other major elements (Ca, Na, K) that are removed from the regolith and this causes the CIA to increase as weathering progresses. Coalescence of etch pits into denticulated margins under appropriate conditions can be accompanied by the precipitation of products within void space (Velbel, 1989), and secondary minerals form by direct replacement of primary chain-silicates (Velbel, 2007; Velbel and Barker, 2008). If alkalis and/or alkaline earths are incorporated into secondary minerals, CIA may increase less than it would if the mobile elements were exported. In some cases the ions in solution change over time as secondary phases precipitate leading to the formation of compositionally different products.

REE and Weathering

REE and trace elements are used by geologists as a tool to interpret magmatic evolution (Hanson, 1989). Geologists attempt to collect the freshest samples but this can be problematic if the changes in volume or other indicators of rock alteration are microscopic (Taylor and Eggleton, 2001). Inadvertent sampling of apparently fresh but subtly weathered samples results in the inclusion of data from altered rock into datasets

intended for petrologic interpretation (Roden et al., 1984; Fodor et al., 1987, 1992; Price et al., 1991; Kushel and Smith, 1992; Cotton et al., 1995).

Previous work has shown that incipient weathering can alter REE signatures (an indication of REE movement during basalt weathering) (Eggleton et al., 1987; Nesbitt and Wilson, 1992; Patino et al., 2003; Sak et al., 2004). REE exist in the REE^{3+} state in solution except for Ce (Wood, 1990; Taylor and Eggleton, 2001). The negative Ce anomalies observed in whole-rock analyses result from oxidation of Ce^{3+} to Ce^{4+} leaving the Ce less mobile compared to other REE^{3+}. The other REE are more easily mobilized and precipitated as secondary REE-rich phases (e.g., phosphates closely associated with primary plagioclase, Wade, 2002). Evidence shows the LREE being preferentially taken up into secondary phases while the HREE are removed from the surrounding regolith in solution (Elderfield et al. 1990; Taylor and Eggleton, 2001). Nesbitt (1979) shows an increase in REE within the outer shells of spheroidally weathered granite. The movement of REE within corestone and spheroidally weathered regoliths will be discussed further in the next section. Whole-rock REE analysis of the corestone 0512008, examined by Wade (2002) and Patino et al. (2003), show an increase in the LREE and a negative Ce anomaly in the rind of the corestone compared to the inner most part of the corestone (Figure 3). Normalization of the rind to the corestone shows that the abundance of Ce in both the corestone and rind of the sample suite is similar. The similarity in Ce abundances demonstrates the relative immobility of Ce during initial weathering and the formation of the negative Ce anomaly.

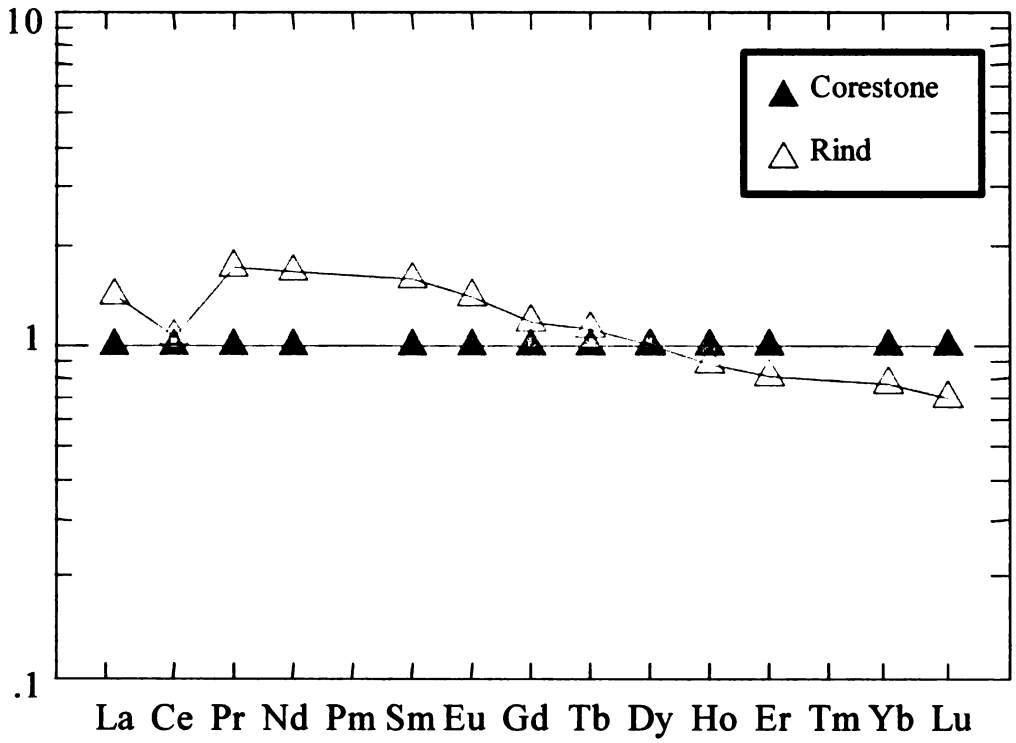

Figure 3. Whole rock REE diagram normalized to the core from sample 0512008 from Wade (2002). The rind shows a negative Ce anomaly (created by the immobility of the Ce in solution) and an increase in the light REE elements above the core abundances caused by weathering.

Spheroidal weathering

Corestones are the least altered volume of rock surrounded by progressively more weathered regolith within a transport limited regime (Ollier, 1971; Carson and Kirkby, 1972; Johnsson, 1993; Taylor and Eggleton, 2001). A transport limited regime is dominated by chemical weathering and lacks the physical removal or transportation of altered material (Carson and Kirkby, 1972; Johnsson, 1993; Taylor and Eggleton, 2001). The alteration of material in place without physical movement of solids, or *in situ* weathering combined with large continuous fractures or other discontinuities (e.g., joints), creates the environment needed for the formation of the corestones. Corestones form as fluid moves through fractures within the rock and begin to weather the rock from the fractures inward toward fresh rock, a phenomenon known as spheroidal weathering (Ollier, 1971; Figure 4). As alteration progresses shells are created around the unaltered core turning the surrounding regolith into saprolite, altered rock that has mostly retained its fresh rock volume (Taylor and Eggleton, 2001).

Each shell surrounding the corestone is at a different stage of alteration and records physical and chemical features of alteration. This allows for analysis of the progressive changes in weathering. Indications of rock alteration are manifested in the form of dissolution features observable with petrography (Stoops et al., 1979) or a scanning electron microscope (SEM) while chemical features are observable as changes in elemental compositions.

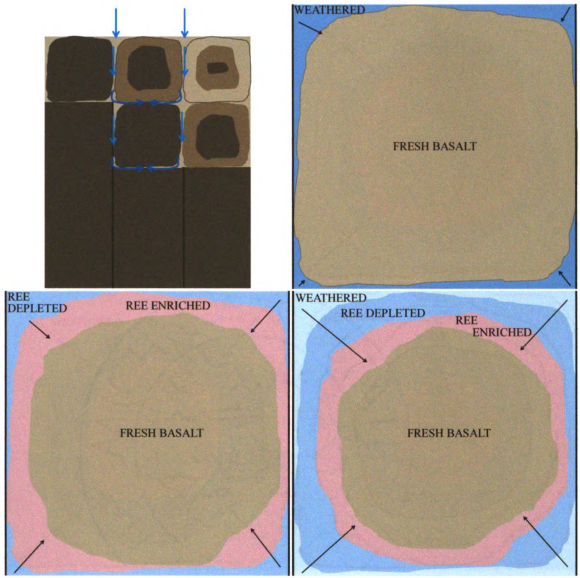

Figure 4. Diagram showing the progression of spheriodal weathering and the relative movement of REE at different stages.

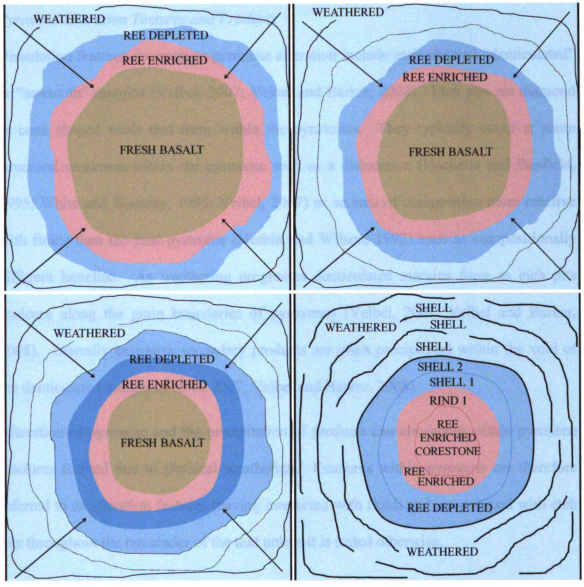

Figure 4 (cont'd).

Pyroxene Alteration Textures and Products

Dissolution features common to pyroxene alteration include etch pits and "denticulated" or "sawtooth" margins (Velbel, 2007; Velbel and Barker, 2008). Etch pits are diamond or cone shaped voids that form within the pyroxenes. They typically occur at some structural weakness within the pyroxene such as a dislocation (Hochella and Banfield, 1995; White and Brantley, 1995; Velbel, 2007) or an area of composition more reactive with fluids than the host pyroxene (Nesbitt and Wilson, 1992) such as compositionally different lamellae. As weathering progresses denticulated margins form as etch pits coalesce along the grain boundaries of pyroxenes (Velbel, 2007; Velbel and Barker, 2008). Laterally extensive secondary products are often precipitated within the void of the denticulated margin (Velbel, 2007; Velbel and Barker, 2008).

Alteration of pyroxene and the precipitation of products can also occur within pyroxene fractures formed due to physical weathering. Fractures within pyroxene are therefore referred to as alteration features (having interacted with fluid) and are grouped with etch pits throughout the remainder of the text unless it is stated otherwise.

GEOLOGIC SETTING

Tecuamburro is a volcanic complex located in southeastern Guatemala and is part of the Central American Volcanic belt, the result of active subduction of the Cocos plate beneath the Caribbean plate (Figure 5) (Cameron, 1998; Cameron et al., 2003; Walker et al., 2003). Tecuamburro is a basaltic to basaltic-andesite composite stratovolcano (Cameron et al., 2003). Tecuamburro is active although it has not erupted during historical times (Reynolds, 1987). Tecuamburro last erupted during the Pleistocene (Reynolds, 1987).

Tecuamburro is located in a tropical climate with an average temperature of 23.4°C and average annual precipitation of 226.08mm (Mitchell et al., 2002). The combination of length of time since the last eruption and climate create the conditions for a sedentary or relict landscape to develop (Johnsson, 1993) within which spheroidal weathering (Ollier, 1971) occurs in the regolith (Taylor and Eggleton, 2001).

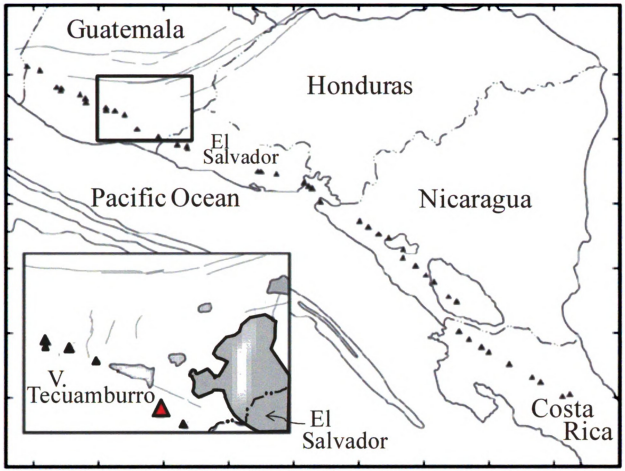

Figure 5. Map of the Central American volcanic arc with an insert to shows the Tecuamburro volcanic complex (red triangle) within Guatemala (adapted from Walker et al., 2003).

Sample Selection

Several corestone and boulder sample suites were collected in 2000 by Barry Cameron, Lina Patino, and Michael Velbel. Sampling within the Tecuamburro volcanic complex included three units (Qas, Qtapg, and Qtap; in order from youngest to oldest unit). Whole-rock geochemical data from Wade (2002) and Patino et al. (2003) were used to select the basaltic andesite corestone-rind pair 0512008 for further geochemical analysis. Corestone system 0512008 is from unit Qtap which has an age of 2.6±0.3 Ma (Reynolds, 1987). A road cut provided access to the corestone, its weathered rind, and surrounding shells of 0512008 within unit Qtap (Figure 6). The landscape surrounding, and above, the sampled site consists of the same unit. From this point on the core and rind of corestone-rind pair 0512008 will be referred to as CC and RCa, respectively.

Both Wade (2002) and Patino et al. (2003) identified movement of REE with the progression of weathering within the 0512008 corestone-rind pair and comparison of them to fresh rock samples from Tecuamburro (Carr Volcanic Database). Figure 7 shows that there is a decrease from corestone to rind in the major elements Si, Na, and K as alteration increases. The corestone falls within the shaded area which highlights the range of possible fresh-rock compositions that have been shown to come from Tecuamburro.

Signs of alteration are present in the whole-rock major elements and REE for corestone system 0512008. The bulk density of the core and rind are similar (~2.2 g/cm^3) and CIAs of the core and rind samples differ only modestly (Figure 8). Both measures indicate that major elements have not been removed from or added to the rind of the corestone-rind system in large quantities (Figure 8). As weathering increases the shells

show a substantial decrease in sample bulk density (<1.4 g/cm^3) and an increase in CIA (from 60-70 in the slightly weathered corestone and rind to nearly 100 – the maximum possible value for CIA – in the shells), implying significant loss of major elements to solution and removal from the regolith.

An initial increase in abundance of the REE occurs from the fresh basaltic andesite through the core and to the rind (Figure 9). The increase in REE in the core and rind is associated with negative Ce anomalies. As weathering progresses abundances of the REE in the shells decrease to below the fresh rock levels with the development of a positive Ce anomaly (Figure 9). REE increases within the core and rind (Figure 9) accompany a minor loss of major elements (Figure 7 and 8), a small range of CIA (Figure 8), and minor change in the core and rind bulk densities (Figure 8). This is interpreted as the occurrence of slight increase in the degree of alteration between the core and rind of the corestone system making this portion of the altered regolith an ideal place to search for incipient alteration of phases.

Figure 6. Images of the corestone system 0512008 and its location within the surrounding regolith (Patino et al., 2003).

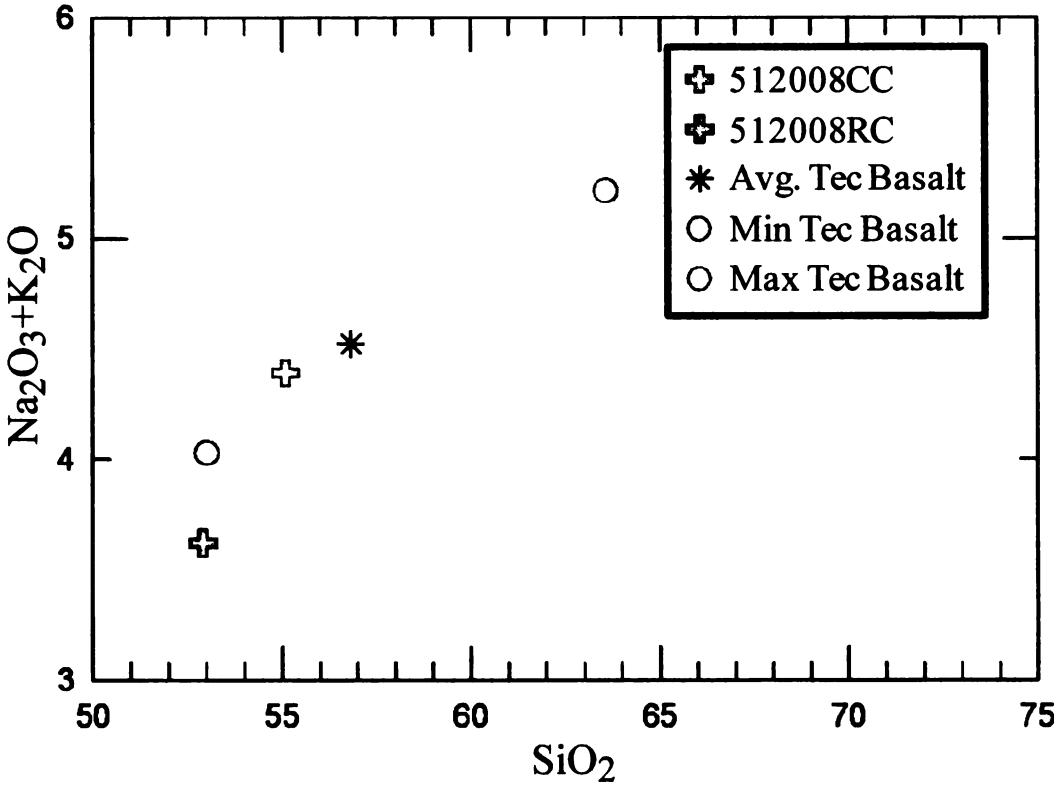

Figure 7. The diagram shows how the corestone and rind plot on a composition diagram. As weathering progresses the fresh rock begins losing SiO_2 and Na_2O+K_2O moving the rind closer to the basalt composition on the diagram. The Tecuamburro (Tec) data was adapted from Carr et al. (2003).

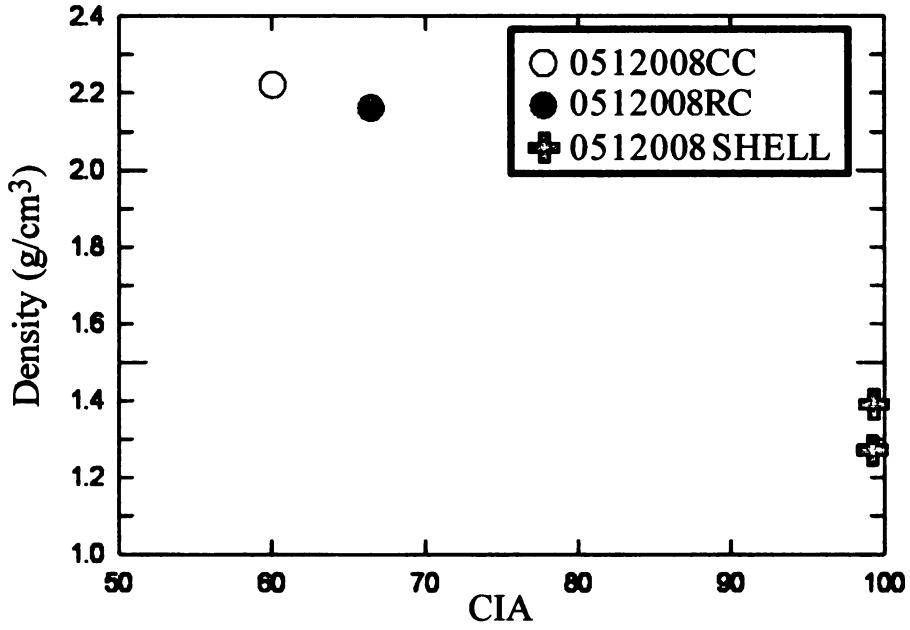

Figure 8. CIA and bulk density diagram for sample 0512008 showing the decrease in density and an increase in CIA with increased weathering.

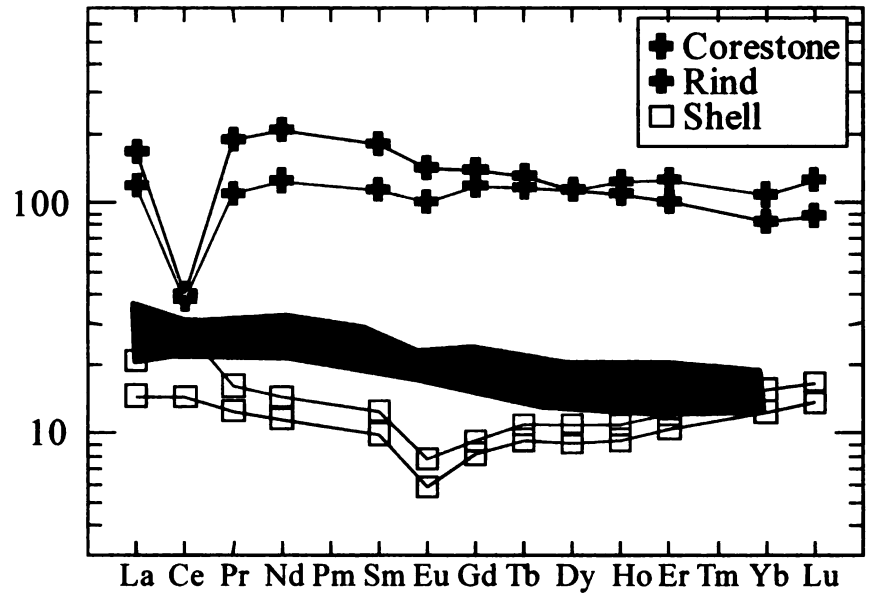

Figure 9. A chondrite normalized REE diagram for 0512008 corestone system re-plotted from Patino et al. (2003). The green region represents the REE of the fresh basalts from the same volcanic center.

METHODS

Petrography

All samples were screened with a petrographic microscope for the presence of pyroxene and then classified by their degree of alteration according to the alteration scale outlined by Stoops et al. (1974), summarized in Figure 10. Figure 11 contains sketches showing the progression of different types of alteration patterns, according to Stoops et al. (1979).

Scanning Electron Microscopy

Samples that were identified as having undergone a low degree of augite alteration, 0-1 as described by Stoops et al. (1979), were examined further for the presence of etch pits using a JEOL JSM-6400V scanning electron microscope at Michigan State University's Center for Advanced Microscopy. Electron microscope images were acquired at operating conditions for the imaging and qualitative analyses of 20kv accelerating voltage, at a working distance of 15mm. Secondary electron images (SEI), backscattered electron images (BEI), and energy-dispersive spectra (EDS) were acquired for multiple augite and enstatite phenocrysts in each sample.

1)	0	1	2	3	4
3) 2)	0-2.5%	2.5-25%	25-75%	75-97.5%	97.5-100%
A	ORIGINAL MINERAL	pellicular	thick pellicular		COMPLETELY ALTERED
			large core	core	
B		irregular linear	irregular banded		
			random residues	random minute residues	
C1		parallel linear	parallel banded		
			organized residues	organized minute residues	
C2		cross linear	cross banded		
			organized residues	Organized minute residues	
D		dotted	patchy		
E			cavernous residue	dispersed minute residues	
		COMPLEX			

1. Degree of alteration (class)
2. Degree of alteration expressed in volume percent
3. Alteration pattern

Figure 10. The above chart breaks up weathering according to Delvigne from Stoops et al. (1979). Pyroxenes in this study follow an irregular linear pattern. Further classification is not necessary because more than 25% alteration does not occur.

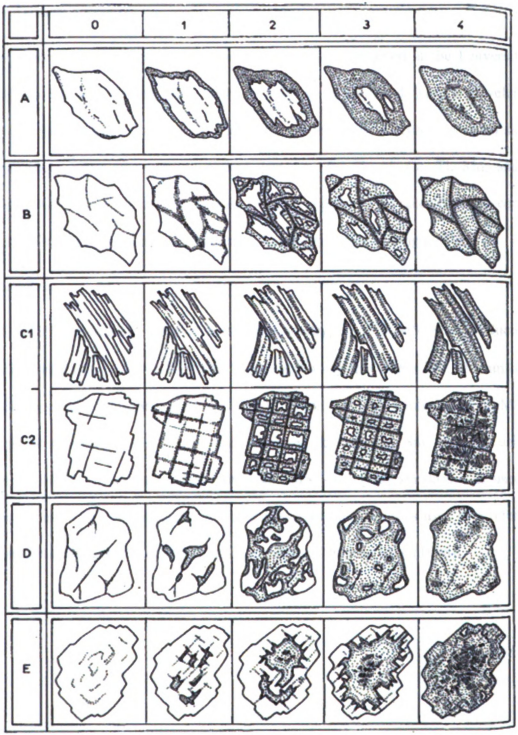

Figure 11. Sketches for different physical manifestations of mineral alteration from Stoops et al. (1979). The corestone and rind pyroxenes from sample 0512008 follow a B alteration pattern, described as irregular linear.

Major Element Analysis

Major element abundances of augite and enstatite were obtained at the University of Michigan's Electron Microbeam Analysis Laboratory equipped with a wavelength-dispersive spectrometer, Cameca SX 100 electron microprobe analyzer. A beam size of approximately 2 μm was used to collect data for Mg, Si, Al, Ca, Ti, Mn, and Fe. Transects with 50-100 μm spacing between analytical points were taken from the cores to the rims of each pyroxene in order to account for the effects of zoning on Ca.

REE Analysis

Laser ablation inductively coupled mass-spectrometry (LA-ICP-MS) was conducted at Michigan State using a Cetac LSX 200^{+} laser ablation system with a UV, 266 nm beam. Pre-ablation was necessary to remove the carbon coating applied for SEM and microprobe analyses. Augite was then analyzed for La, Ce, Sm, and Nd using a frequency of 10 Hz and a 50 μm spot size. NIST-612 glass standard was used for calibration and calcium (as determined by microprobe analysis) was used as a reference element in calculating the concentrations according to Norman et al. (1996).

RESULTS

Petrographic Results

The majority of pyroxenes in 0512008 are subhedral to euhedral phenocrysts in a glassy matrix. Several samples contain pyroxenes with opaque inclusions. Petrographic images of augite from CC and RCa can be found in the 0512008 Corestone Pyroxene Images of Appendix A.

Augite (identification confirmed by electron probe microanalysis; see below) grains in samples CC and RCa are classified as 0 according to Stoops et al. (1979), showing less than 2.5% alteration (Figure 10). Pyroxenes in both samples have an irregular linear alteration pattern according to the classification scheme from Stoops et al. (1979) (Figure 11).

SEM Results

Petrographic identification and characterization of incipient alteration features within the pyroxene are difficult due to the minute size of the features being investigated. Features present at the beginning of alteration will naturally be microscopic and grow in size as weathering progresses. Features such as etch pits may therefore be difficult to identify by thin-section petrography. In these cases SEM analysis is necessary to confirm the presence of, and characterize, the etch pits. Chains of etch pits appeared in pyroxene as long (5-20 μm) "strings of beads" or short, spatially recurring groups of voids (1-5 μm) in the grain depending on their size (Figure 12).

BEI reveal the presence of high Z-contrast lamellae running parallel to and intersecting the *en echelon* etch pits in several augites (Figures 13 & 14). Increasing the

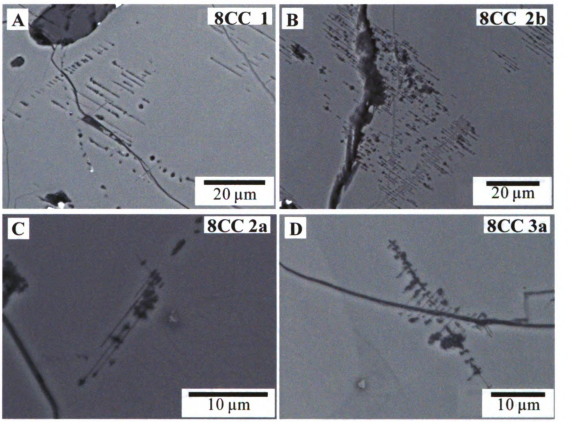

Figure 12. BEI (A-J) of etch pits within augite and enstatite phenocrysts from Guatemalan corestone sample 0512008. Images A-H are from core pyroxenes and I-J from rind pyroxenes.

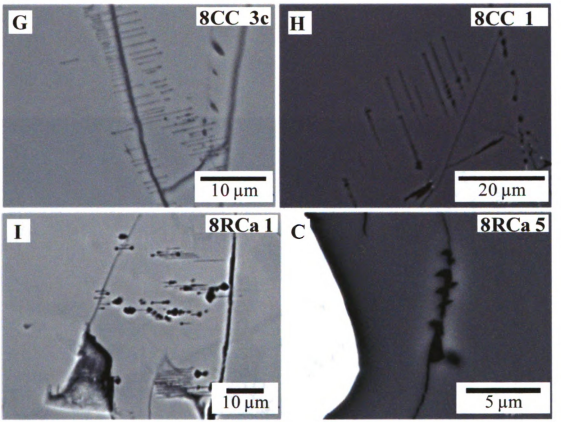

Figure 12 (cont'd).

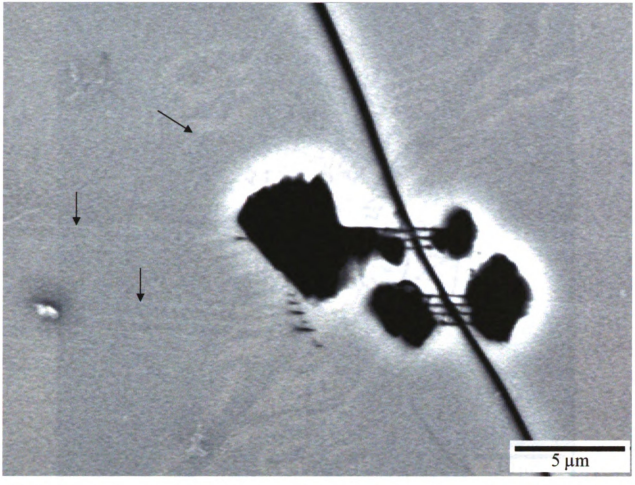

Figure 13. Backscattered electron image of etch pits intersecting parallel to high Z-contrast lamellae from sample RCa-1. Arrows are perpendicular to the lamellae.

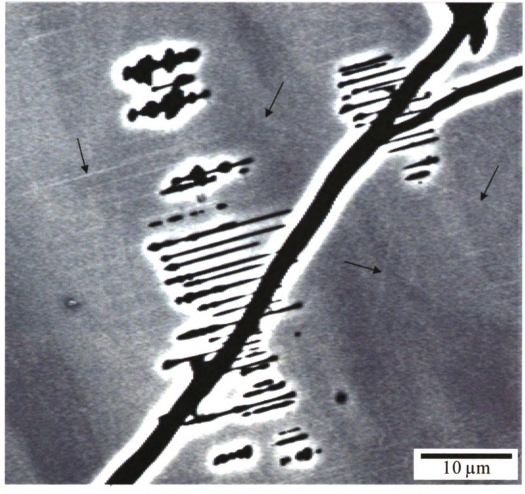

Figure 14. Multiple directions of lamellae shown in the BEI image from sample CC-6. The contrast has been increased for easier identification of the lamellae. Arrows are perpendicular to and point out location of several lamellae. Exsolution textures can also be seen running from northwest to southeast.

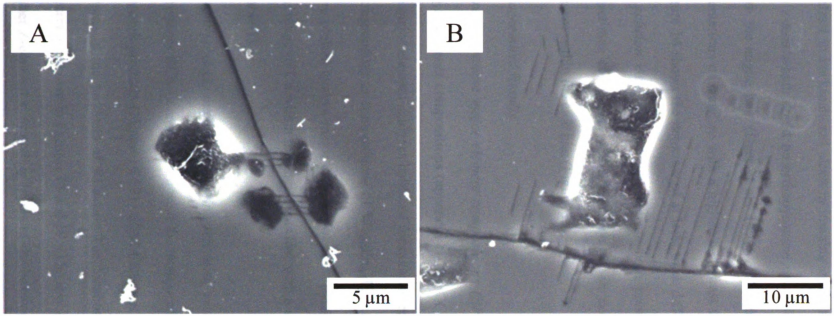

Figure 15. SEI of etch pits filled with a secondary product from sample (A) RCa-1 and (B) RCa-8.

contrast in backscattered electron imaging mode reveals exsolution lamellae parallel to the z-axis which could be orthopyroxene or a clinopyroxene of composition different from the augite host (Deer et al., 1997). The stretched contrast also reveals multiple orientations of lamellae with a higher Z-contrast than the surrounding "host" pyroxene. Figure 14 shows the presence of at least three different orientations of lamellae. Where *en echelon* etch pits and lamellae are both present the lamellae are parallel to, and sometimes contiguous with, the arrays of *en echelon* etch pits. SEI show products present within the etch pits (Figure 15).

Geochemical Results

Parent pyroxene major-element compositions (EPMA) – Microprobe analysis provided major element compositions (appendix B) for CC and RCa augite and enstatite. Using the major element analyses balanced formulae were calculated for the augite and enstatite corresponding to compositions of $Wo_{40}En_{44}Fs_{16}$ and $Wo_3En_{60}Fs_{37}$ respectively. Data were plotted against major elements of other pyroxenes from Tecuamburro (Figure 21). The range of Ca within the augite was low with a span between 7.16-8.35 atomic percent (Table 1).

Parent-product major- and minor-element compositional relations (SEM-EDS) – Pyroxenes RCa-1a and RCa-1b were the most weathered and exhibited laterally extensive boxwork products (Figure 16-17). SEM-EDS was used to qualitatively identify elements present in the products of RCa-1a. The locations of analyses and the corresponding spectra are shown in Figures 18 and 19. The low Z-contrast material, central parting and higher Z-contrast surrounding layers of the boxwork all contained Al, Si, Ca, Ti, and Fe.

A few products within various pyroxenes were probed for the major elements present (phosphorus was not analyzed) and the data are plotted on ternary diagrams in Figure 20.

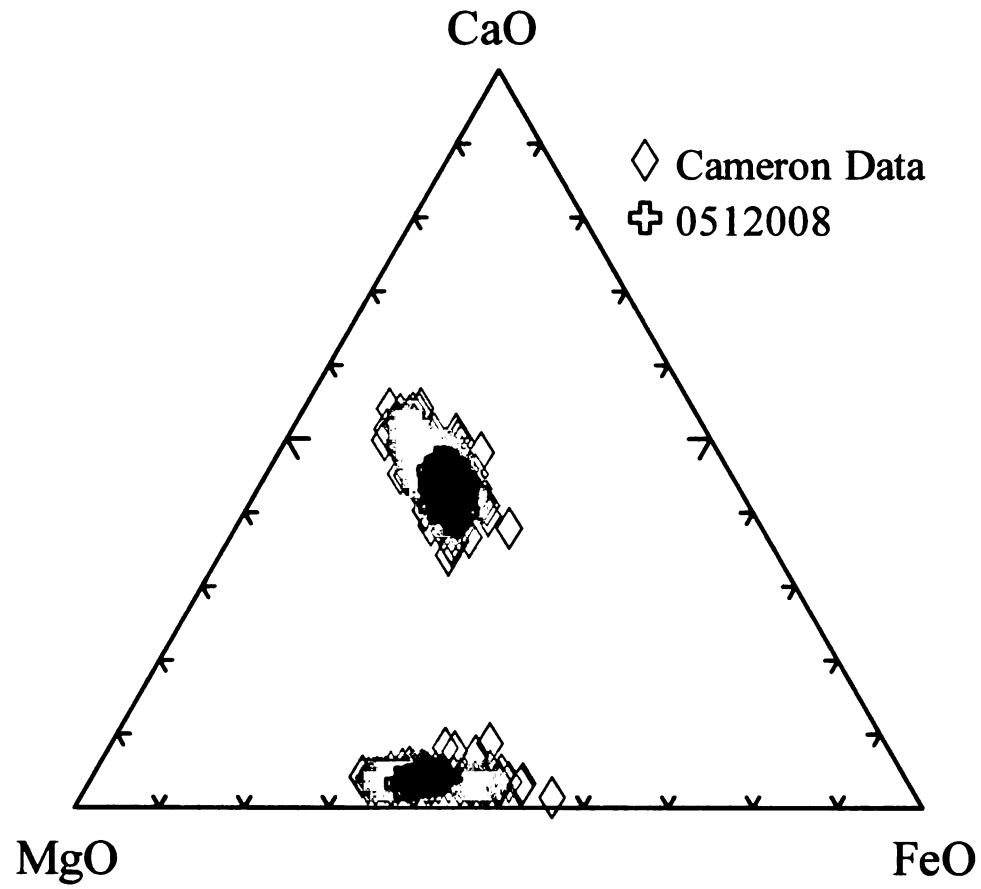

Figure 16. Ternary diagrams of pyroxene microprobe results from Barry Cameron and corestone system 0512008. Results for corestone system 0512008 are consistent with other pyroxene compositions from Guatemala (Cameron data).

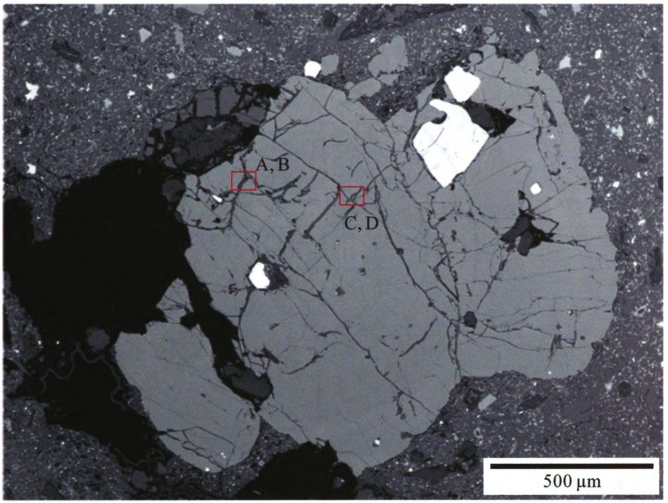

Figure 17. Advanced alteration pyroxene forming denticulated margins with laterally extensive boxwork and voids on an augite in the rind of RCa-1. Boxes show the locations of images (A, B) and (C, D) in Figure 17.

Figure 17. Advanced alteration pyroxene forming denticulated margins with laterally extensive boxwork and voids on an augite in the rind of RCa-1. Boxes show the locations of images (A, B) and (C, D) in Figure 17.

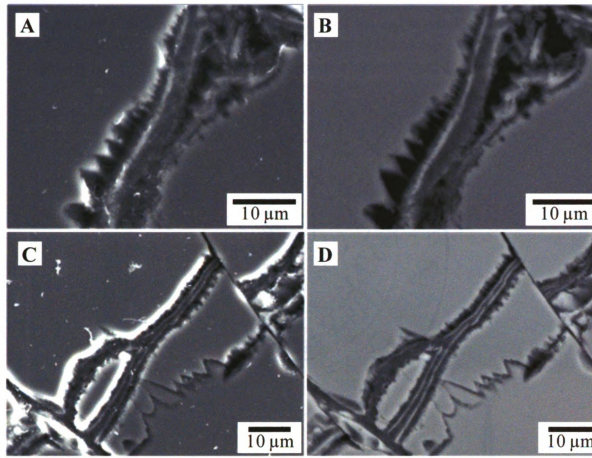

Figure 18. Secondary (A, B) and BEI (B,D) images from pyroxene RCa-1a in Figure 16 showing the presence of laterally extensive boxwork products and denticles. B and D show the presence of a low contrast central parting of a secondary product encased by a higher contrast product. Both areas show the presence of sawtooth denticles and peripheral voids.

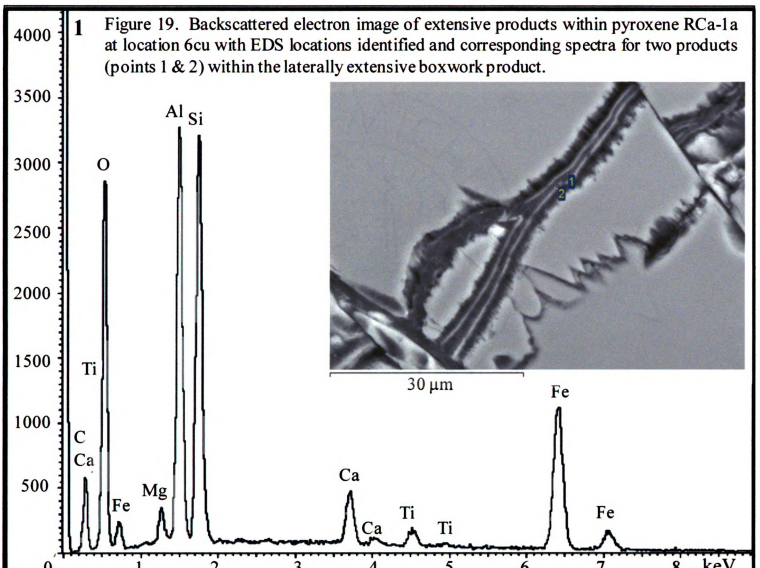

Figure 19. Backscattered electron image of extensive products within pyroxene RCa-1a at location 6cu with EDS locations identified and corresponding spectra for two products (points 1 & 2) within the laterally extensive boxwork product.

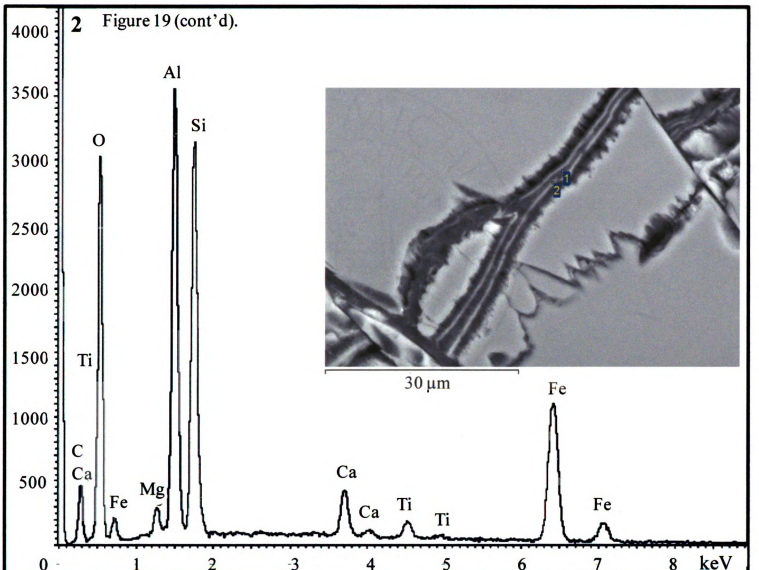
2
Figure 19 (cont'd).
4000
3500
3000
2500
2000
1500
1000
500
0
1
2
3
4
5
6
7
8
keV
Al
Si
O
Ti
C
Ca
Fe
Mg
Ca
Ca
Ti
Ti
Fe
Fe
30 µm

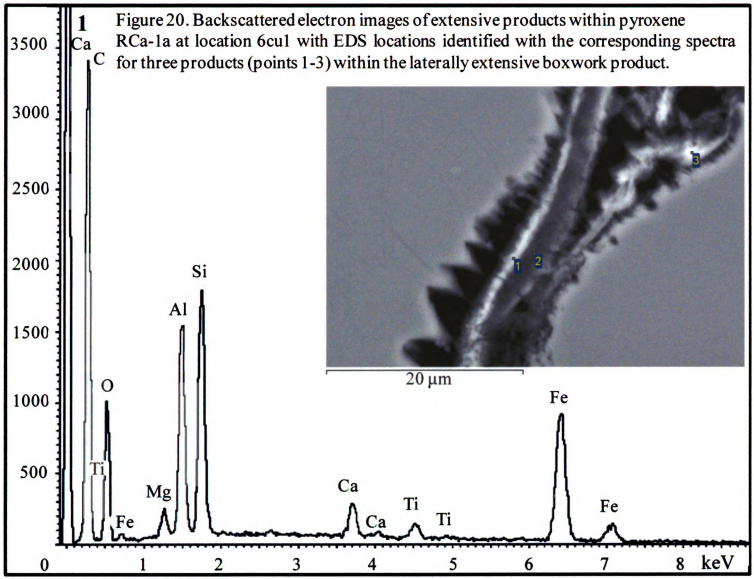

Figure 20. Backscattered electron images of extensive products within pyroxene RCa-1a at location 6cu1 with EDS locations identified with the corresponding spectra for three products (points 1-3) within the laterally extensive boxwork product.

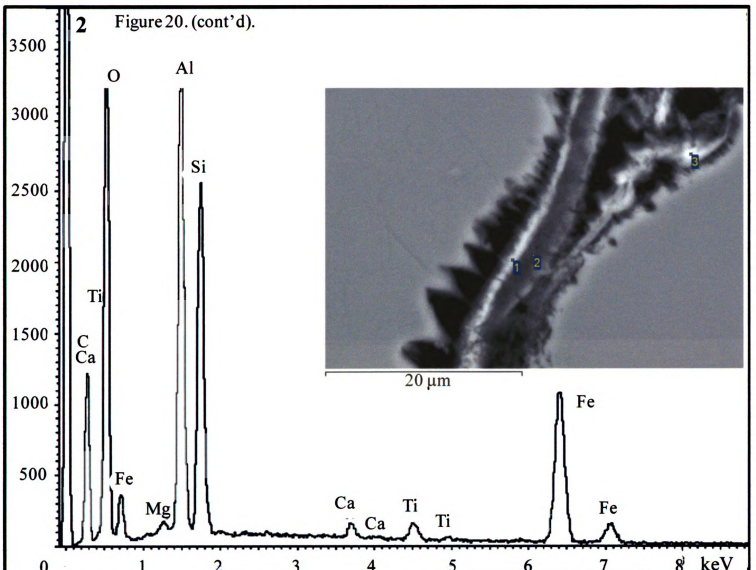
2
Figure 20. (cont'd).
3500
3000
2500
2000
1500
1000
500
0
1
2
3
4
5
6
7
8
keV
O
Al
Si
Ti
C
Ca
Fe
Mg
Ca
Ca
Ti
Ti
Fe
Fe
20 µm

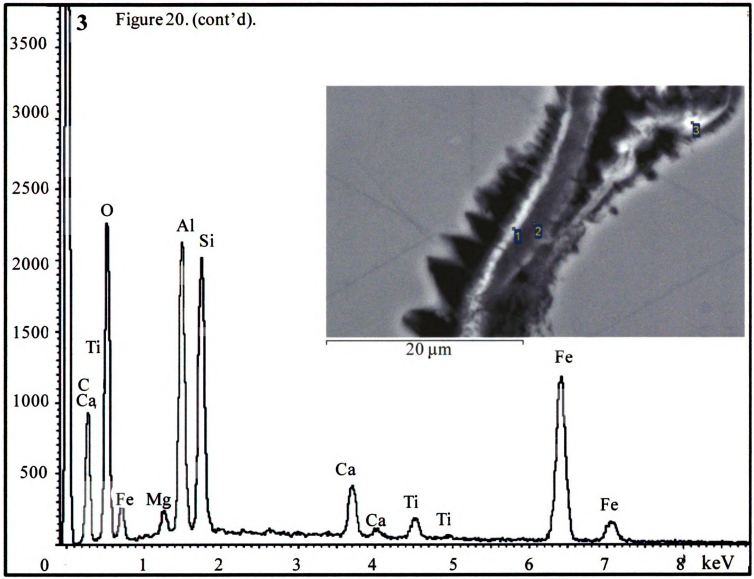

Figure 20. (cont'd).

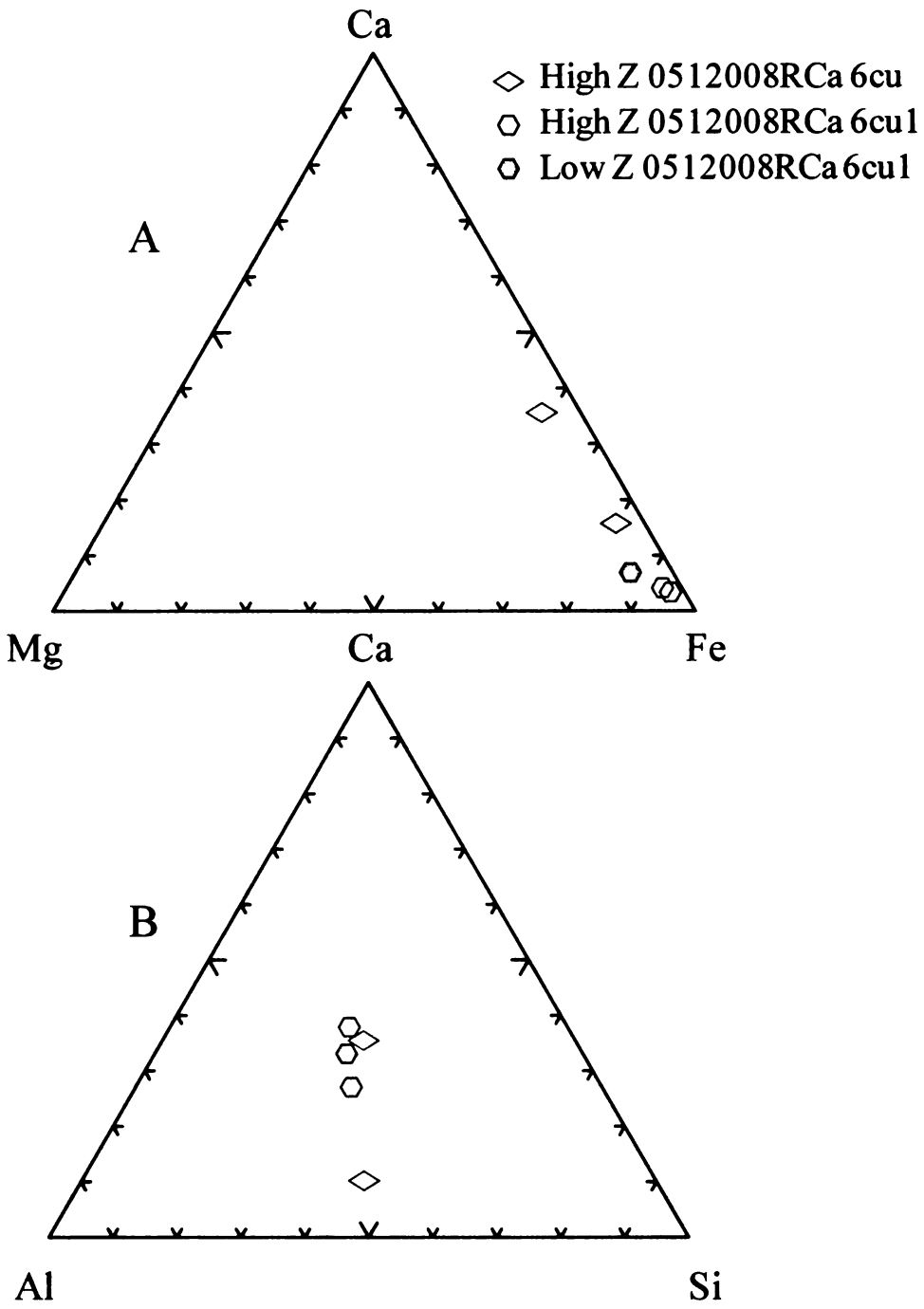

Figure 21. Ternary diagrams plotting the compositions of the products in Table 1 and Figures 18 and 19 as determined by microprobe analysis.

Minor and trace-element compositions of pyroxenes and products (LA-ICP-MS) – To avoid problems created by zoning and its effect on analyses of Ca (the internal standard) the LA-ICP-MS analyses were acquired along the microprobe transect and matched to the nearest microprobe analysis. The standard deviation for the Ca was less than 1.0% when standards were run (Appendix C) and the ranges of elements abundances detected are shown in Table 1.

REE DATA RANGES

	Sm	Nd	Ce	La	Ca
Mean	0.26	3.41	1.30	0.35	7.87
Median	0.00	3.26	1.26	0.35	7.93
Max Value	1.66	16.04	1.88	4.14	8.35
Low Value	0.00	1.70	0.73	0.00	7.16

Table 1. Average, median, minimum, and maximum values measured for the LREE (ppm) and Ca (atomic percent) measured by LA-ICP-MS.

REE analyses were restricted to the augite phenocrysts due to the low abundances of LREE in orthopyroxenes, which were below detection capabilities of the mass spectrometer. The 30 μm thickness of thin sections limited the amount of material that could be ablated and limited analysis to four REE; La, Ce, Nd, and Sm. These four elements were chosen based on Patino et al.'s (2003) results that identified increases in the LREE abundances and the presence of negative Ce anomalies in whole-rock analyses.

A total of 21 augites were analyzed for REE and plotted on a normalized REE diagram (Figure 22). A total of 89 ablation points of unaltered or altered (etch pits and fractures present) locations were analyzed by LA-ICP-MS (appendix B). Several of the ablation craters revealed that the etch pits seen on the polished surface of the thin-section actually extended beneath the thin sections' pre-ablation surface of the pyroxene. Examination of other ablation craters revealed augite alteration below pre-ablation thin-section surfaces which were not visible before ablation (removal) of surface material. These "subsurface" alteration features including etch pits, fractures, and products were uncovered once the augite was ablated away (Figures 23-25). This led to reclassification of several ablation locations: augites that were etch-pit free pre-ablation surfaces were reclassified as containing etch pits if ablation exposed subsurface pits. A total of 41 ablation locations with "alteration" were identified; two with a product (or possibly a primary inclusion) present, 15 containing etch pits, 17 with fractures, and 7 with etch pits and a fracture (Figure 26). Figure 27 shows the samples with enriched LREE and negative Ce anomalies and indicates what type of alteration is associated with the analyzed ablation crater.

Pyroxene CC-2b, from the core of 0512008, contains two ablation craters with enriched LREE and negative Ce anomalies (Figure 28). The ablation crater near the rim (point CC-2b-1) of the pyroxene and the area around etch pits in the center (point CC-2b-e) have enriched LREE with a negative Ce anomaly. Post-ablation BEI show a small fracture is crosscutting point 1 and that the etch pits at point e extend into the thin-section, below pre-ablation surface of the pyroxene (Figure 29).

Ablation crater CC-1a-m-4 (Figure 29) also shows a negative Ce anomaly and the REE are enriched by approximately three orders of magnitude in La, Nd and Sm relative to the surrounding pyroxene (Figure 30). SEM examination of the ablation crater after ablation shows the presence of a high Z-contrast (high atomic number) inclusion. A negative Ce anomaly is also associated with augite CC-3 from the corestone (Figure 31). The ablation crater associated with the Ce anomaly is crosscut by a fracture and etch pits (Figure 32). The REE diagram (Figure 32) shows the negative Ce anomaly appears to result from an increase in La compared to other locations within the same pyroxene.

Three Ce anomalies were identified within the rind of sample RCa. Figure 33 is a BEI image of a cluster of pyroxenes with one of the augites (circled in the image) containing a negative Ce anomaly. Figure 34 is an enlarged image of ablation crater RCa-2a-2-1 that reveals the presence of a crosscutting fracture and etch pits visible within the ablation crater and the REE diagram with a negative Ce anomaly. Figure 35 shows the location of RCa-1a and RCa-1b. An enlarged image of ablation craters RCa-1b-3 and RCa-1b-4 and a plot of REE data for all augite RCa-1b craters are in Figure 36. Ablation craters two and three have fractures associated with them, while ablation crater four has both a fracture and etch pits. Figure 37 is an enlarged image of ablation crater RCa-1a-1 and the REE diagram for RCa-1a data, which indicate a crosscutting fracture is associated with the negative Ce anomaly. Both ablation craters RCa-1a-1 and RCa-1b-4 have negative Ce anomalies associated with fractures.

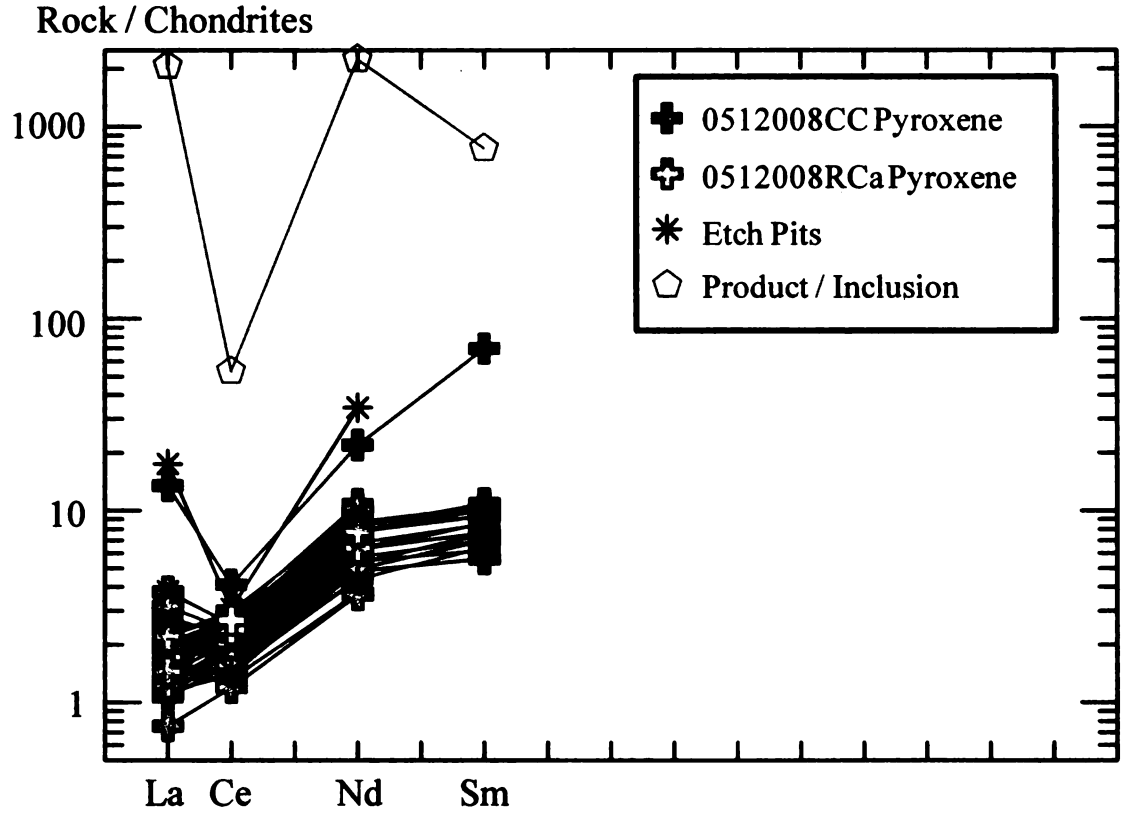

Figure 22. REE diagram with all LA-ICP-MS LREE data for CC and RCa pyroxenes. Classification of the symbols are: 0512008CC and 051200RCa Pyroxene denotes that the analysis was done on a core or rind augite with no etch pits or products present, Etch Pits indicate that the surface analyzed contained etch pits, and Product/Inclusion indicates that the analysis included a product of inclusion.

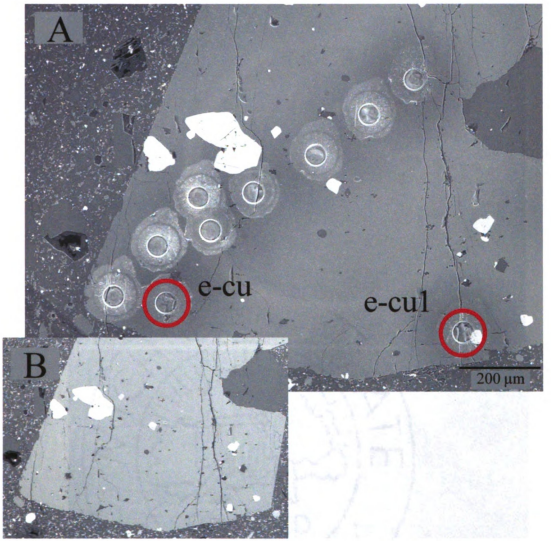

Figure 23. BEI of sample pyroxene RCa-3. (A) Identifies the post-ablation locations (circled) for points RCa-3e-cu and RCa-3e-cu1 that contain etch pits. (B) Image of RCa-3 surface before ablation.

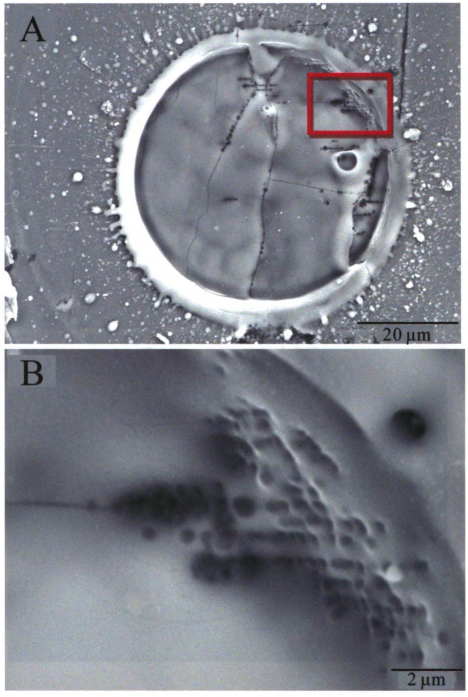

Figure 24. (A) BEI image of post-ablation crater RCa-3e-cu with numerous etch pits present. (B) BEI image of an inset from image A showing an enlarged view of the etch pits. The edge of the ablation crater reveals that the etch pits extend from the surface of the thin section down to the bottom of the crater.

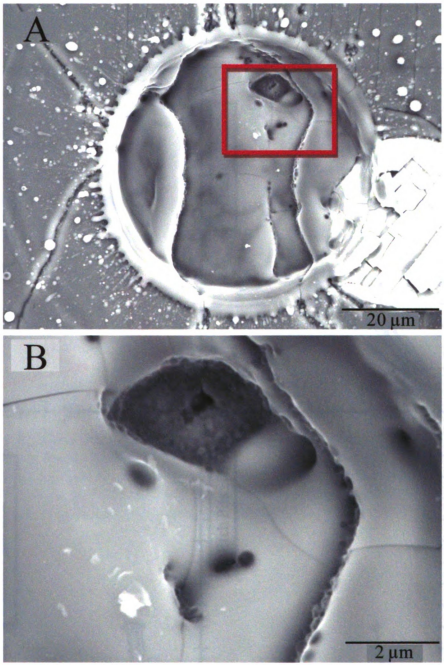

Figure 25. (A) BEI image of post-ablation etch pit RCa-3e-cu1. (B) BEI image of the inset from image A revealing subsurface etch pits.

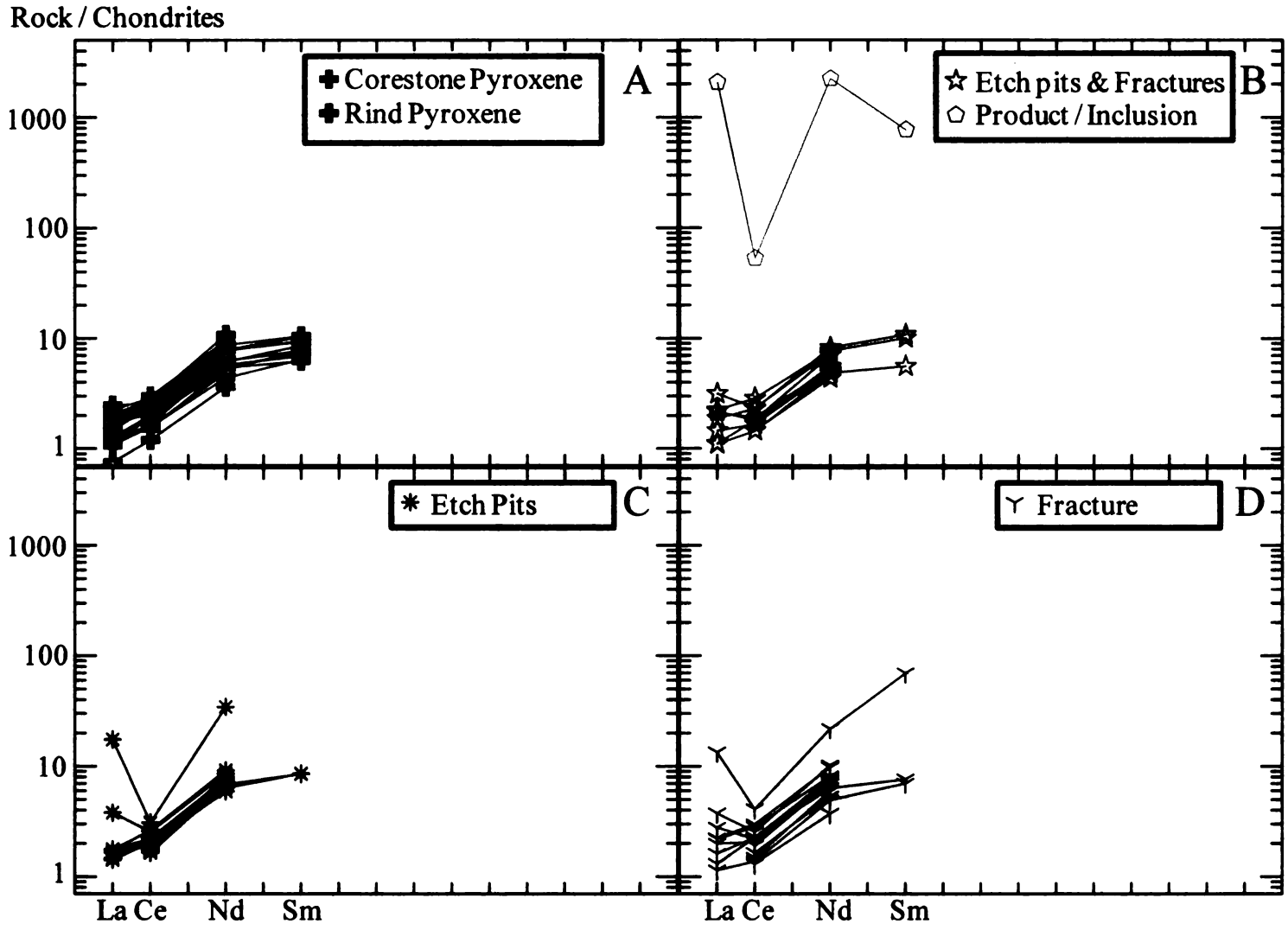

Figure 26. LREE diagrams with data sorted into fresh or no alteration present, both etch pits and fractures present, etch pits present, and fractures present. The corestone or rind classification identifies the location of the pyroxene in the corestone.

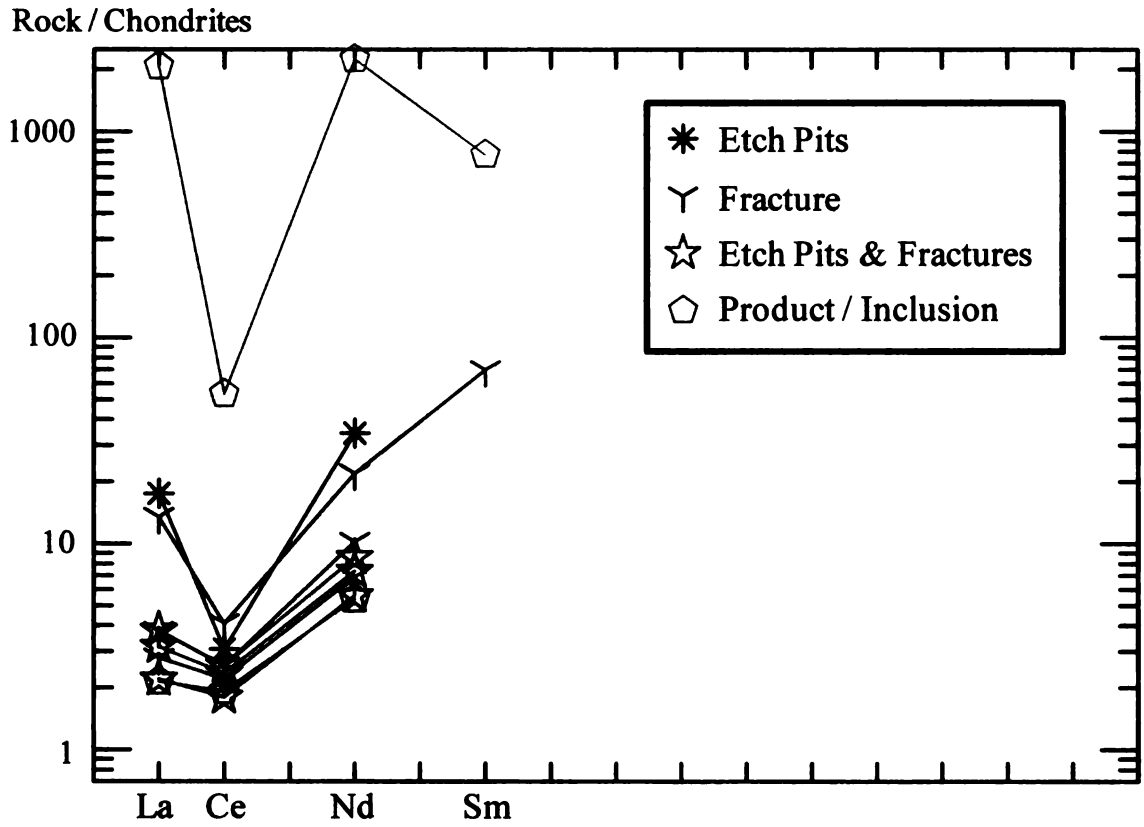

Figure 27. LREE diagram normalized to Chondrites showing the pyroxene analyses with negative Ce anomalies present. Classification of the symbols are: Rim denotes the analysis was taken at the edge of the pyroxene, Corestone and Rind denote the location of the pyroxene within the sample, Etch Pits indicate that the surface analyzed contained etch pits, and Product/Inclusion indicates that the analysis included a product of inclusion.

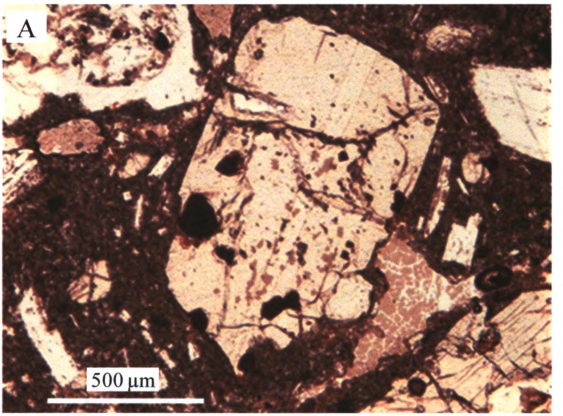

Figure 28. Image (A) is a petrographic image of augite CC-2b, (B) is a backscattered electron image showing the location of the transect of ablation craters, (C) shows the augite before ablation. The REE diagram shows the negative Ce anomalies associated with CC-2b-1 and CC-2b-e.

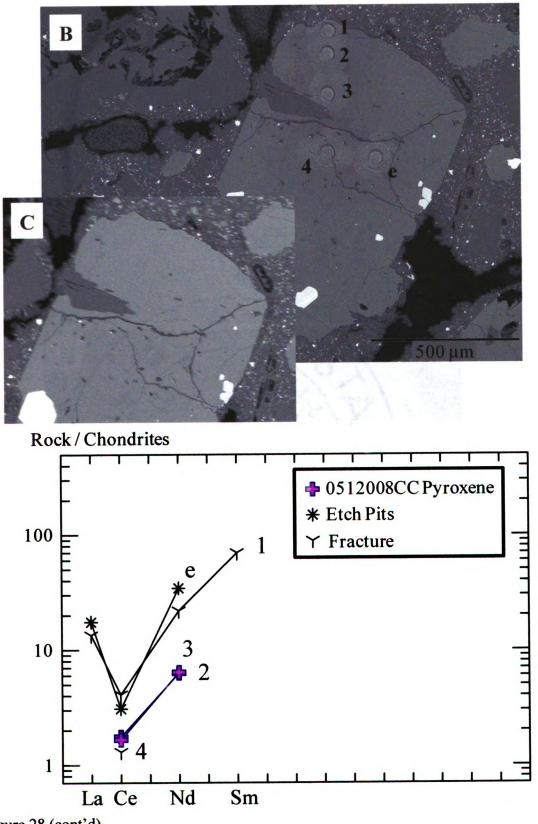

Figure 28 (cont'd).

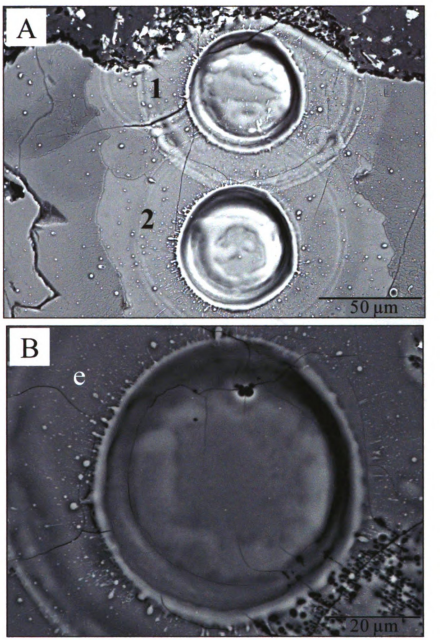

Figure 29. BEI of ablation craters CC-2b-1, CC-2b-2, and CC-2b-e (Figure 28). (A) A fracture is cutting through the upper left corner of CC-2b-1. No alteration features are visible in CC-2b-2. (B) BEI image of ablation crater CC-2b-e with multiple etch pits visible within the top and lower right corner of the ablation crater.

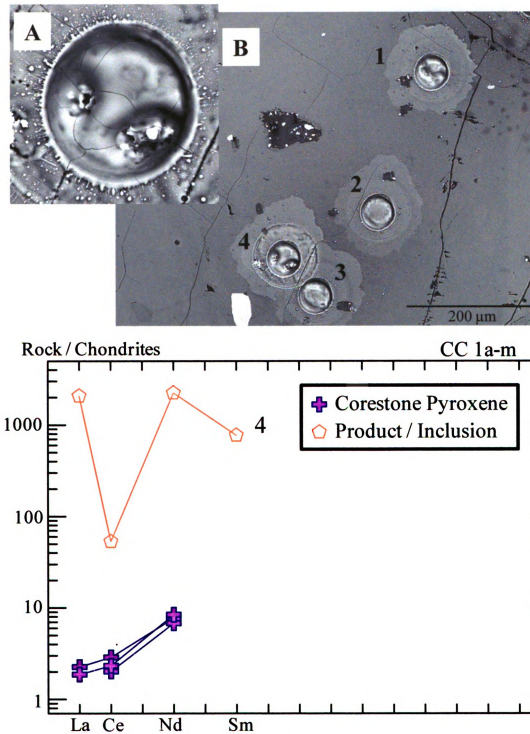

Figure 30. (A) and (B) are backscattered electron images of the ablation craters from the augite CC-1a-m from Figure 29. (A) is a close up of crater 4 showing the presence of a white, high Z-contrast phase. (B) contains the other ablation craters within the pyroxene. The REE diagram for the ablation craters shows a high abundance of La, Ce, Nd, and Sm compared to other locations within the same pyroxene and contains a negative Ce anomaly.

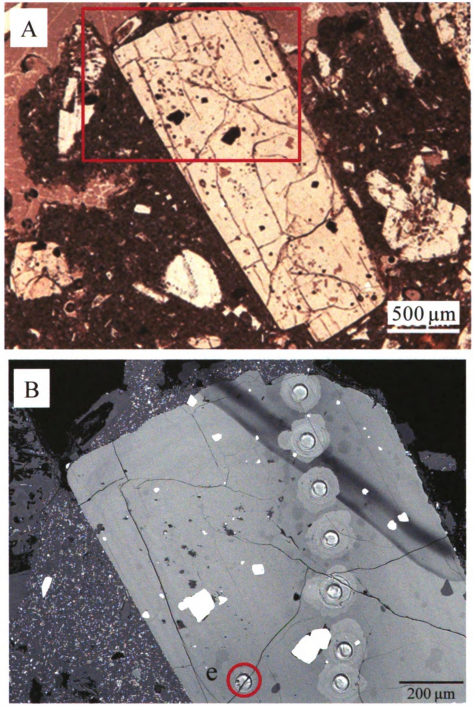

Figure 31. (A) Petrographic and (B) backscattered electron image of an augite, CC-3, from the corestone. Image B is a close up of the inset from A showing the location of ablation crater CC-3-e and the fracture that crosscuts it.

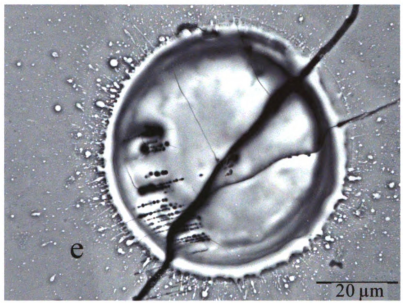

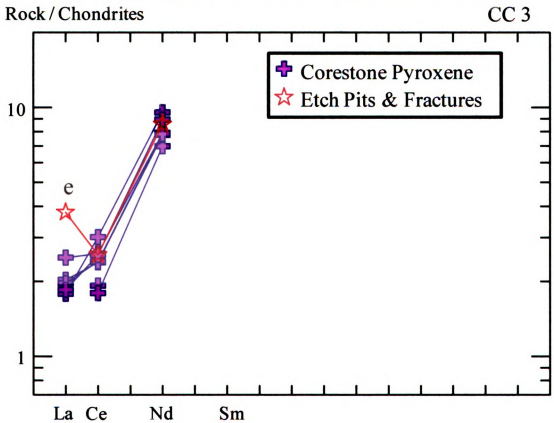

Figure 32. Backscattered electron image of a close up of CC-3-e from Figure 31 and shows a fracture and etch pits within the ablation crater. The REE diagram shows the negative Ce anomaly associated with the ablation crater. Other ablation craters within the same augite showed an increase in La to Nd with no negative Ce anomalies.

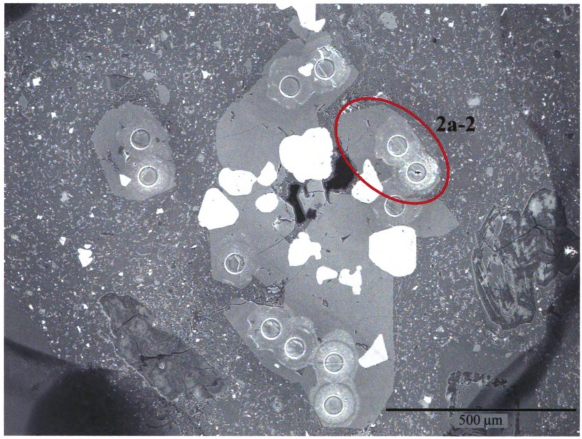

Figure 33. The backscattered electron image shows the location of ablation craters in augite RCa-2a-2.

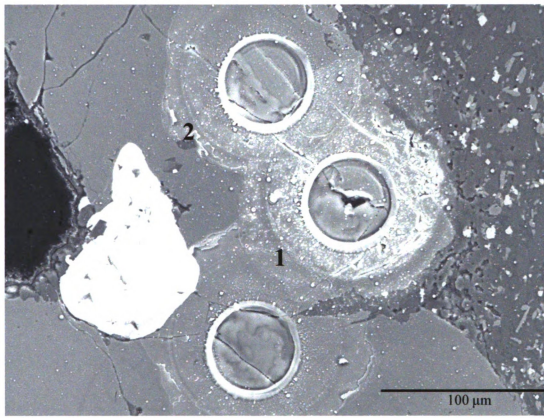

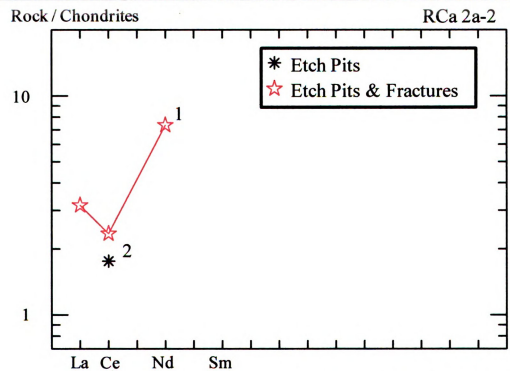

Figure 34. The backscattered electron image is an inset of Figure 33 showing ablation craters RCa-2a-1 and RCa-2a-2. A negative Ce anomaly is shown on the REE diagram for RCa-2a-1 and only Ce was detectable in RCa-2a-2.

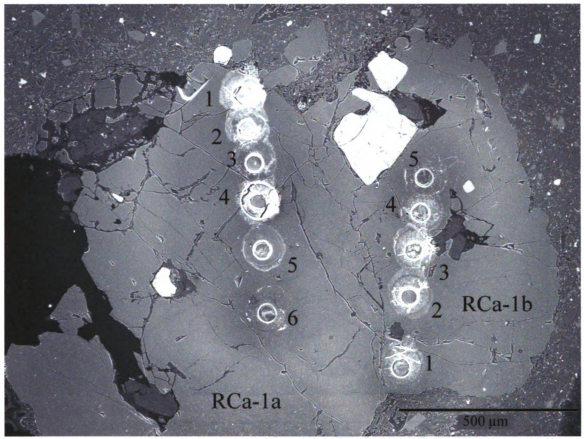

Figure 35. Backscattered electron image of two augites RCa-1a and RCa-1b showing transects of ablation craters.

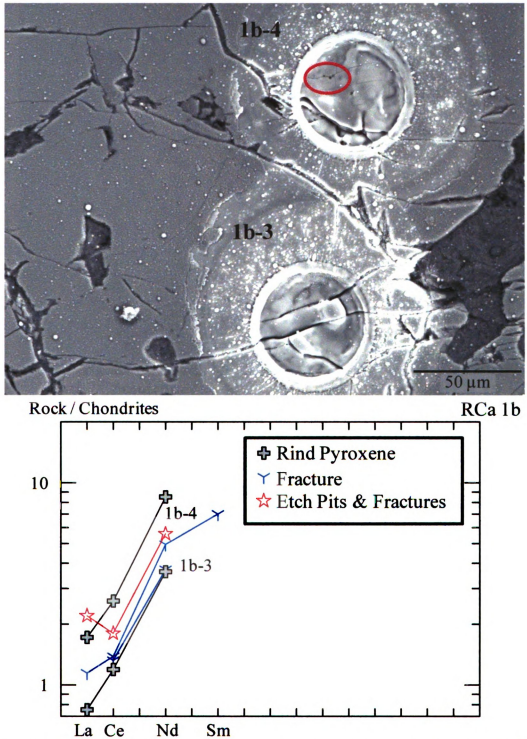

Figure 36. The backscattered electron image is an inset of Figure 35 showing ablation craters RCa-1b-3 and RCa-1b-4. Visible fractures crosscut both ablation craters and remnants of ablated etch pits can be seen within the circled area of RCa-1b-4. The chondrite normalized REE diagram shows data for all ablation craters in augite RCa-1b with RCa-1b-3 and RCa-1b-4 labeled. There is a negative Ce anomaly associated with RCa-1b-4.

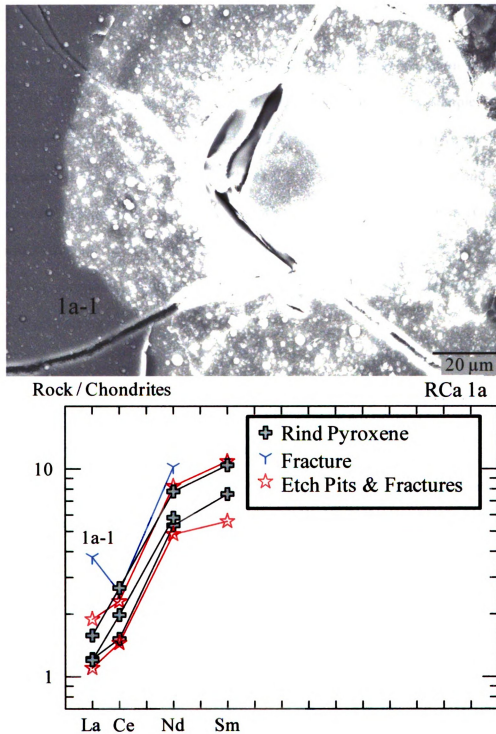

Figure 37. The backscattered electron image from RCa-1a-1 shows visible fractures that crosscut the ablation crater. The chondrite normalized REE diagram shows data for all ablation craters in augite RCa-1a with the negative Ce anomaly associated with RCa-1a-1 labeled and in blue.

DISCUSSION

A connection has been established between the onset of physical alteration features and changes in LREE signatures of corestone and rind augites from sample 0512008. Observations show an increase in LREE and the presence of a negative Ce anomaly accompanies the first stages of augite alteration with the LREE decreasing and negative Ce anomaly disappearing with subsequent alteration of augite from Guatemala. Characterization of the REE behavior during incipient alteration of augite within the Guatemalan corestones provides a better understanding of the geochemical changes during spheroidal weathering.

Etch pits

Etch pits appear to be the first visually observable sign of pyroxene alteration. The etch pits within pyroxenes of the 0512008 corestone-rind pair appear to be associated with, or located near, a fracture. This is consistent with a well-established understanding that fractures are a typical conduit used by fluids to gain access to the more weathering-susceptible areas of the pyroxene, as noted by Stoops et al. (1979). Etch pits were found in both 8CC (core) and 8RCa (rind). Etch pits in the former were generally $\leq 1\mu m$ (in width, from side to side) and in the latter $>1\mu m$, as exhibited in Figure 29. The more alteration a grain has undergone the larger the etch pits are (Velbel, 2007) with the largest etch pits occurring in the more weathered material (in this case, the weathered rind).

Further information on the formation and occurrence of etch pits during alteration of augite grains was provided by comparing pre- and post-ablation imaging of the laser ablation craters. The observation of etch pits in post ablation images is cause for caution

when classifying samples according to their degree of alteration as imaged in SEM-BEI. Within the samples studied, several visible etch pits were apparent in pyroxenes prior to ablation and numerous additional etch pits were found upon ablation. Therefore, visible estimations of alteration need to be thought of as a general estimate when approximating the extent of alteration within pyroxene grains. In this instance the pyroxenes were thought to be only slightly weathered and chosen to represent the first stages of weathering. Ablation of pyroxenes with no pre-ablation "surface" etch pits that were originally classified as fresh led to the discovery of post-ablation "subsurface" etch pits, requiring reclassification of those grains from fresh to altered.

Some etch pits are located in areas associated with chemical in homogeneities within the pyroxenes, near intra- and inter-mineral fractures. High Z-contrast lamellae identified by BEI imaging appear to be preferentially weathered over the host augite, leading to the formation of *en echelon* etch pits (Figures 27-28). Attempts to constrain the composition of the lamellae using SEM-EDS spectra, microprobe and LA-ICP-MS analyses were unsuccessful. This is due to the submicron size of the lamellae and the beam diameters of the analytical techniques used, which prevented the analysis of the thin lamellae without including surrounding (host) pyroxene. Higher-spatial resolution methods (e.g., transmission electron microscopy) are required to characterize these lamellae.

Enriched LREE and Negative Ce Anomalies

Seven ablation craters exhibit enriched LREE and negative Ce anomalies; CC-2b-1, CC-2b-e, CC-3-e, CC-1a-m-4, RCa-1a-1, RCa-1b-4 and RCa-2a-2-1. Each of these seven ablation craters are spatially associated with alteration features (i.e., fractures and/or etch pits). The enriched LREE and negative Ce anomalies could be a primary feature of the

pyroxenes, caused by an inclusion in the augite, or they could be secondary, resulting from precipitation of a LREE enriched product into the voids created by augite alteration. The partitioning of the LREE creates an increase in abundances from La to Sm without the presence of a Ce anomaly and rules out the possibility of the LREE signature being primary. The lack of inclusions within ablation craters during pre- and post-ablation inspection eliminates inclusions as an explanation for the LREE signature. This leaves the precipitation of the LREE enriched product within the voids as the cause of the enriched LREE and negative Ce anomalies in the seven augites. (Ce is less mobile and provides less cations that can be incorporated into the product, therefore causing the negative Ce anomaly.)

Forty-one ablation craters were identified as containing some form of alteration (i.e., fractures, etch pits, or both) but only seven ablation craters (4 CC and 3 RCa) have the LREE enrichment and negative Ce anomaly. A possible interpretation is that the increase in REE is associated with incipient alteration (i.e., fractures and/or etch pits) of the augite and as later stages of alteration are reached the abundance of LREE is depleted causing the LREE signature to look similar to fresh augite values.

The lack of increased LREE abundances and a negative Ce anomaly within other ablated areas with visible alteration could be explained in one of two ways. First is the absence of LREE enriched products within the alteration features. This could be due to alteration being almost negligible (in the initial stages of alteration) or the solution that is interacting with the augite is depleted in dissolved cations that would be precipitated as products with enriched LREE. The second possibility is that a LREE-bearing product has

been completely removed (leaving the voids empty; the LREE signature would then be that of fresh augite) or replaced by a tertiary product low in LREE.

Determining which of the possible explanations apply requires highly detailed pre-ablation imaging of the fractures and etch pits (which was not done here) to look for the presence or absence of a product. Pre-ablation identification is difficult because etch pits must be located with an SEM to determine whether there are products present, and then find those same etch pits must subsequently be relocated using a petrographic microscope during ablation analyses. This makes is difficult to locate and ablate specific etch pits. Post-ablation inspection is not useful in answering this question because products (if they were present to contribute to the LA-ICP-MS analyses) have been ablated away before post-ablation inspection.

Augite weathering in spheroidally weathered corestones and rinds

Weathering increases from the corestone outward towards the rinds of a spheroidally weathered corestone. As weathering advances the bulk density of the sample decreases while the CIA increases. Unlike the unidirectional progression of the aforementioned characteristics, REE abundances of the corestone system initially increase and are later depleted. The LREE behavior of altered augite in the 0512008 corestone system mimics the whole-rock REE behavior of this corestone system and others as shown by Patino et al. (2003).

Comparison of the LREE signatures of the fresh, core (CC) and rind (RCa) augites (Figure 26) shows no differences. The progression of rock alteration creates zones of alteration within which alteration varies somewhat between different mineral-grain-scale microenvironments, sometimes even in different parts of a single grain (e.g., near

fractures versus near grain boundaries) resulting in overlapping degrees of alteration for the same mineral in the most-weathered core and the least-weathered rind. There is therefore not a one-to-one correspondence between where the augite is (core or rind) and the incipient or more altered LREE signatures observed within that grain. This could explain the overlapping of core and rind LREE signatures, in that the pyroxenes examined are all from different spatial locations within the core or rind and all have different spatial relations to intra- and inter-mineral fractures. This makes the distinction between some core and rind microenvironments less definitive than expected from simplified models of alteration as far as the geochemical characteristics of the varying microenvironments in the core and rind are concerned.

It is possible to interpret the LREE signatures for the core and rind augites by classifying their degree of alteration using textural alteration features and geochemical data together in order to eliminate the problems created by overlapping zones of alteration. Areas within pyroxenes that have no signs of textural alteration are classified as fresh, those with etch pits, fractures, or some other void (pore space) and an elevated LREE signature with a negative Ce anomaly are incipiently weathered, and those areas with textural indications of alteration but "fresh" augite LREE signatures (low LREE abundance and no Ce anomaly) are more extensively weathered.

Contribution of pyroxenes to REE enrichment

The original hypothesis being tested by this study was that weathering of clinopyroxenes contributed to previously reported increases in whole-rock REE (Patino et al., 2003). Substitution of Ca ions by REE is expected in Ca-bearing clinopyroxenes, due to the similar ionic radii of Ca and the REE (McKay, 1989; James et al., 2002). Experimental

studies of pyroxene dissolution kinetics have shown that Ca is one of the first major elements to be removed during pyroxene alteration (Brantley and Chen, 1995); simultaneous release of REE from sites with similar crystal chemistry might be expected. However, the results of this study indicate that the main role of clinopyroxene weathering in REE redistribution is not as a source of REE that are mobilized during incipient weathering. Instead, incipiently weathered clinopyroxene appears to serve as an early-weathering host-phase for alteration microenvironments within which are precipitated secondary minerals enriched in LREE derived from other minerals.

The contribution of augite and enstatite to the increased whole-rock abundance of REE and associated negative Ce anomalies is negligible. Enstatite has a low abundance of REE due to its low REE partition coefficients and contributes little to no REE to the whole-rock signature of the corestone system (McKay, 1989; Onuma et al., 1968). Augite has higher REE partition coefficients and therefore a higher REE abundance (McKay, 1989; Onuma et al., 1968) but there was no indication from the geochemical data of this study that the augite contains enough REE to have supplied the high abundances of LREE observed associated with void spaces in the weathered augite.

The presence of secondary products with an increased abundance of LREE within the void spaces of weathered augites suggests that, rather than augite contributing REE to the whole-rock abundances, the voids within weathered augites provide an appropriate microenvironment for (as yet unidentified) REE-enriched products to precipitate out of solution. A number of previous workers have suggested that the products which host the

majority of REE are secondary phosphates (Banfield and Eggleton, 1989; Wade, 2002; Patino et al., 2003), but other secondary minerals besides phosphates can also serve as REE hosts, and the specific identity of the secondary REE-host minerals required to account for the results of this study cannot be determined on the basis of the available data.

Possible REE sources for LREE enrichment

The likely sources of REE to REE-enriched corestones (e.g., Patino et al., 2003) and LREE-enriched microenvironments within weathered augites (this study) include nearby primary phases that begin weathering before pyroxene (short-range sources), or REE host phases external to the corestone-rind system (long-range sources). Plagioclase is highly altered within some SE Guatemalan corestone systems, and plagioclase hosts REE-rich phases (Wade, 2002). Weathering of the plagioclase explains the presence of kaolinite and halloysite shown by Wade (2002). A solution interacting with plagioclase comes into contact with and exposes REE-rich inclusions that may serve as possible sources of REE. In appropriate microenvironments, solutions might be saturated with respect to various secondary minerals that could precipitate (e.g., kaolinite and halloysite, as observed by Wade, 2002) in voids of plagioclase and pyroxene. Some such microenvironments might similarly be conducive to precipitation of secondary REE-host minerals. While such short-range sources may be applicable to this study, plagioclase phenocrysts like those reported by Wade (2002) are not abundant in the samples examined for this study, so other REE-source minerals must be considered. Patino et al. (2003) suggested larger-scale (within-regolith) redistribution of REE into corestone-rind

complexes from elsewhere in the regolith. Volcanic glass or mineral hosts for phosphates (Banfield and Eggleton, 1989; Nesbitt and Wilson, 1992) could be the main long-range contributors to the elevated whole-rock REE content of the corestone system.

CONCLUSIONS

SEM images of augites from corestone system 0512008 show a consistent progression of alteration during weathering. Weathering begins with the formation of etch pits at or near fractures, in some instances enhanced along compositionally distinct lamellae. Continued weathering produces denticulated margins, some with extensive boxwork products filling laterally extensive void space. Geochemical analysis of volumes of weathered core and rind augites including etch pits and fractures reveal higher abundances of La and in some instances Nd and Sm as well, when compared to unaltered augite. This increase in these LREE is interpreted as being caused by the incorporation of REE into secondary phases which precipitate within the newly formed voids. Some analyses of etch pits and fractures lack the increase in LREE and the negative Ce anomaly. The lack of LREE and negative Ce anomaly in these instances may indicate that the initial REE-enriched secondary products formed during early weathering are removed later as tertiary products are formed.

Pyroxene is not a primary source of LREE that contributes to the increased REE whole-rock abundances of the corestone system 0512008. Pyroxene does not contribute LREE to whole-rock abundances as a source, but serves as a host for LREE enriched secondary phases. Weathering and dissolution of pyroxene create void space (etch pits and fractures) which provide an ideal location for the precipitation of the inferred LREE enriched (with negative Ce anomalies) products.

APPENDIX A

PYROXENE PETROGRAPHY

PHASES/TEXTURES IDENTIFIED BY PETROGRAPHY

THIN SECTIONS Corestone System 051200-	8A	8B	8C1	8CC	8CRC	8CRR	8RC	8RCa	RCb
MINERALS									
Clinopyroxene		x	x	x	x	x	x	x	x
Orthopyroxene		?	x	x	x	x	x	x	x
Olivine	x		x	x	?	x	x	x	x
Iddingsite	x		x	x		x	x	x	x
Opaque, Glass, Plagioclase		x	x	x	x	x	x	x	x
Orange Product							?		
Brown Product			x	?		?		x	x
TEXTURES									
Degree of Weathering		0	0	0	0	0	0	0	0
Fractures			ra		ra	ra	ra	ra	ra
Etches						x		x	
Denticles				?		?/s			s
Boxwork Products								?	

SYMBOLS (Degree of Weathering and Fractures descriptions for the degree and type of alteration are taken from Stoops et al. (1979))

0	**ra**	**s**	**?**
(<2.5% alteration)	(intramineral fractures)	(small etches)	(maybe present/very small)

Table 2. The table shows the phases and different alteration textures that were identified using a petrographic microscope for several core and rind locations within corestone system 0512008.

0512008-CC and -RCa CORESTONE SYSTEM PYROXENE IMAGES

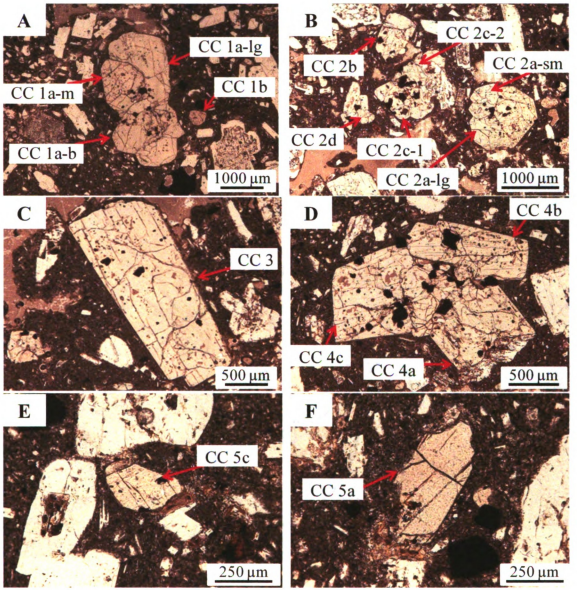

Figure 38. Petrographic images (plane and crossed polarized light) of augite and enstatite grains from the core and rind of sample 0512008. Images (A-H) are from the corestone and (I-N) are from the weathered rind of the corestone. Arrows indicate the location of and composition of each pyroxene examined in this study.

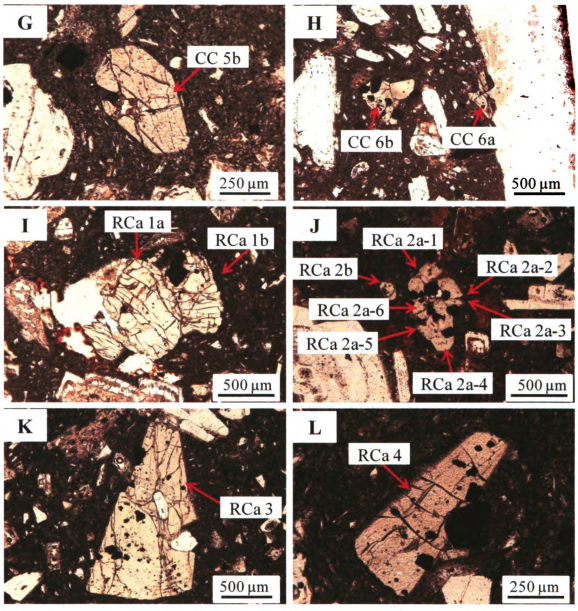

Figure 38 (cont'd).

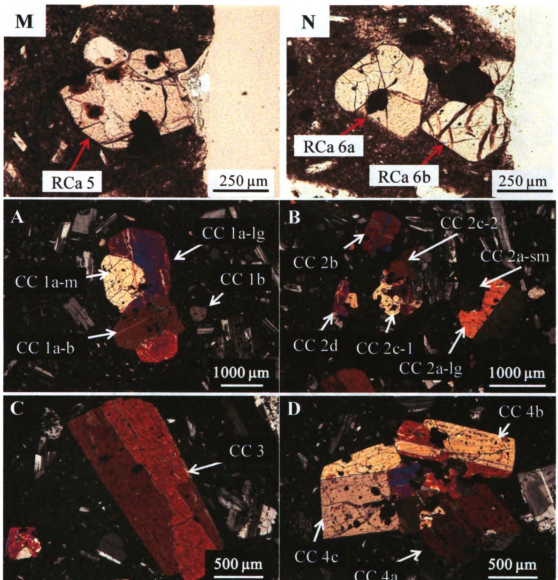

Figure 38 (cont'd).

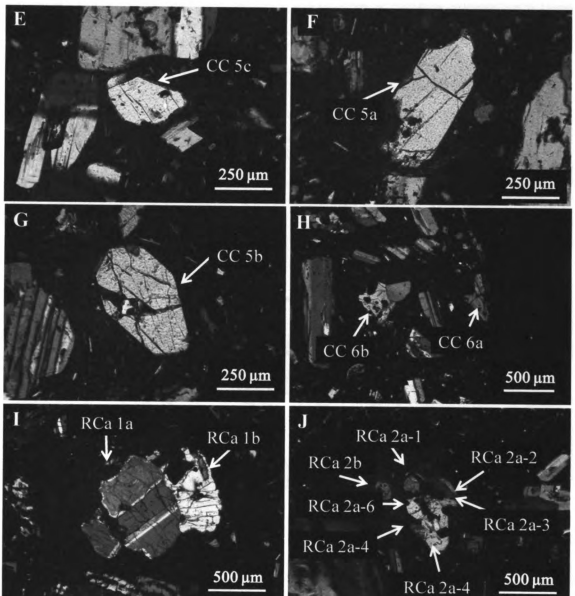

Figure 38 (cont'd).

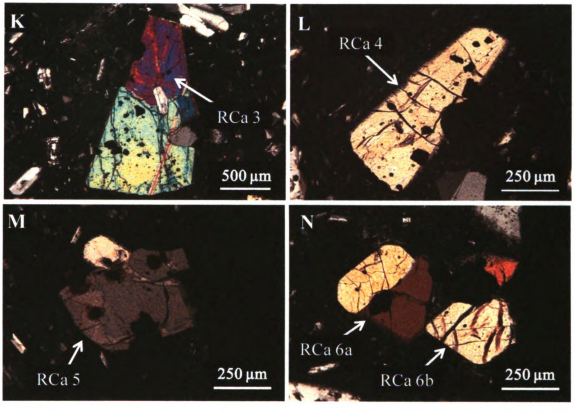

Figure 38 (cont'd).

APPENDIX B

MICROPROBE AND LA-ICP-MS PYROXENE ANALYSES
FOR SAMPLE 0512008

AUGITE GEOCHEMICAL DATA

										*(ppm)			
Sample	**Ca**	**Mg**	**Fe**	**Na**	**Al**	**Mn**	**Ti**	**Si**	**O**	**La***	**Ce***	**Nd***	**Sm***
CC-1a-lg-1	8.07	8.38	3.18	0.27	1.13	0.12	0.17	18.92	59.76	0.46	1.67	4.08	1.60
CC-1a-lg-2	8.02	8.79	2.91	0.23	0.81	0.12	0.18	19.13	59.80	0.30	1.23	2.93	1.17
CC-1a-lg-3	8.22	8.36	3.07	0.27	1.29	0.13	0.22	18.72	59.73	0.29	1.13	2.53	0.95
CC-1a-lg-4	8.04	8.17	3.30	0.26	1.20	0.13	0.17	18.94	59.79	0.25	1.20	2.69	1.06
CC-1a-lg-5	7.70	8.74	2.98	0.29	1.25	0.12	0.12	19.00	59.80	0.26	0.96	2.05	0.98
CC-1a-m-1	8.26	8.50	2.99	0.29	1.09	0.11	0.14	18.91	59.72	0.53	1.76	3.60	-
CC-1a-m-2	8.06	8.48	3.21	0.26	0.99	0.12	0.14	18.98	59.74	-	1.24	3.17	-
CC-1a-m-3	7.92	8.75	3.08	0.22	0.87	0.13	0.14	19.10	59.78	0.44	1.42	3.93	-
CC-1a-m-4	7.92	8.75	3.08	0.22	0.87	0.13	0.14	19.10	59.78	491.80	32.57	1047.63	118.08
CC-1a-b-1	8.22	8.24	2.86	0.27	1.57	0.09	0.17	18.77	59.80	0.34	1.23	2.98	1.31
CC-1a-b-2	8.25	8.25	2.92	0.29	1.46	0.09	0.17	18.79	59.77	0.35	1.38	3.17	1.30
CC-1a-b-3	7.94	8.49	3.19	0.27	1.07	0.13	0.17	18.98	59.77	0.31	0.97	2.35	-
CC-1a-e	7.60	8.53	3.42	0.24	1.15	0.13	0.17	18.96	59.79	0.39	1.24	3.74	-
CC-2a-lg-1	8.00	8.33	3.18	0.25	1.15	0.11	0.16	19.01	59.81	0.40	1.32	3.52	-
CC-2a-lg-2	7.87	8.26	3.35	0.27	1.44	0.13	0.18	18.75	59.76	0.46	1.72	5.04	-
CC-2a-lg-3	7.87	8.80	3.05	0.20	0.84	0.13	0.13	19.17	59.81	-	1.37	3.75	-
CC-2a-lg-4	7.96	8.80	3.01	0.20	0.89	0.12	0.13	19.10	59.79	-	1.05	-	-
CC-2a-sm-1	7.34	9.00	3.22	0.22	0.86	0.14	0.12	19.26	59.85	-	1.07	-	-
CC-2a-sm-2	7.72	8.56	3.32	0.24	1.06	0.12	0.13	19.06	59.80	-	1.12	3.28	-
CC-2a-sm-3	7.37	8.92	3.48	0.21	0.93	0.15	0.16	19.02	59.77	-	1.01	3.18	-
CC-2b-1	7.91	8.58	3.19	0.25	1.01	0.12	0.15	19.01	59.77	3.19	2.51	10.23	10.68

Table 3. Major and minor element abundances of areas within augite from corestone system 0512008.

Sample	Ca	Mg	Fe	Na	Al	Mn	Ti	Si	O	(*) ppm La*	Ce*	Nd*	Sm*
CC-2b-2	7.91	8.58	3.19	0.25	1.01	0.12	0.15	19.01	59.77	-	1.07	2.93	-
CC-2b-3	7.68	8.90	3.26	0.22	0.78	0.13	0.12	19.15	59.77	-	1.01	2.98	-
CC-2b-4	8.13	8.51	3.00	0.25	1.06	0.11	0.13	19.03	59.79	-	0.80	-	-
CC-2b-e	7.31	9.07	3.41	0.20	0.77	0.15	0.12	19.18	59.79	4.14	1.88	16.04	-
CC-2c-1-1	8.15	8.67	2.71	0.25	1.30	0.10	0.13	18.91	59.78	-	1.01	2.49	-
CC-2c-1-2	8.07	8.55	3.02	0.24	1.33	0.10	0.19	18.77	59.75	0.66	1.35	3.22	-
CC-2c-1-3	7.98	8.64	3.01	0.24	1.18	0.11	0.17	18.91	59.77	0.31	1.38	2.97	1.17
CC-2c-1-4	8.35	8.33	2.75	0.27	1.58	0.10	0.18	18.69	59.76	0.39	1.43	2.89	1.31
CC-2c-2-1	7.87	8.72	2.89	0.23	1.44	0.08	0.16	18.83	59.80	0.27	1.10	2.54	-
CC-2c-2-3	8.25	8.30	3.07	0.23	1.55	0.11	0.21	18.57	59.72	0.47	1.26	3.46	-
CC-2c-2-4	7.95	8.45	3.10	0.25	1.52	0.13	0.18	18.69	59.75	0.53	1.76	3.58	1.54
CC-2d-1	7.65	8.93	3.12	0.19	0.90	0.13	0.11	19.15	59.81	-	1.42	-	-
CC-2d-2	7.64	8.56	3.42	0.25	0.98	0.13	0.12	19.10	59.79	-	1.14	3.04	-
CC-2d-3	7.99	8.16	3.39	0.28	1.42	0.12	0.19	18.73	59.74	0.48	1.53	3.67	-
CC-3-1	7.78	8.66	3.23	0.26	0.93	0.13	0.14	19.10	59.79	-	1.18	-	-
CC-3-2	7.91	8.69	3.11	0.21	0.92	0.13	0.14	19.10	59.79	-	1.10	3.26	-
CC-3-3	7.86	8.44	3.27	0.23	1.24	0.12	0.16	18.90	59.78	0.48	1.46	3.62	-
CC-3-4	7.84	8.64	3.17	0.21	0.91	0.13	0.13	19.16	59.82	0.59	1.58	3.69	-
CC-3-5	8.12	8.42	3.16	0.24	1.07	0.12	0.15	18.96	59.76	0.42	1.84	4.46	-
CC-3-6	8.00	8.58	3.12	0.21	1.06	0.11	0.16	18.99	59.78	0.47	1.47	3.65	-
CC-3-7	8.01	8.39	3.21	0.27	1.36	0.12	0.16	18.76	59.73	0.44	1.56	4.17	-

Table 3 (cont'd).

Sample	Ca	Mg	Fe	Na	Al	Mn	Ti	Si	O	(*) ppm La*	Ce*	Nd*	Sm*
CC-3-e	7.53	8.56	3.57	0.11	1.09	0.16	0.15	19.01	59.83	0.90	1.56	4.00	-
CC-4a-1	7.53	8.76	3.04	0.39	1.35	0.13	0.14	18.90	59.76	0.34	1.25	3.11	-
CC-4a-2	7.63	8.75	3.29	0.23	0.97	0.13	0.14	19.07	59.79	0.38	1.33	3.55	-
CC-4a-3	7.52	8.68	3.42	0.23	1.21	0.14	0.16	18.87	59.77	-	1.31	4.03	-
CC-4a-4	7.93	8.50	3.15	0.25	1.29	0.11	0.17	18.84	59.76	-	1.20	3.32	-
CC-4a-5	7.90	8.38	3.26	0.26	1.45	0.13	0.20	18.69	59.74	0.38	1.36	3.28	-
CC-4a-6	7.92	8.39	3.22	0.23	1.27	0.13	0.20	18.86	59.79	0.52	1.74	3.80	-
CC-4a-7	8.07	8.46	3.13	0.23	1.20	0.12	0.17	18.87	59.76	0.53	1.83	4.58	-
CC-4b-1	7.51	8.71	3.42	0.23	1.33	0.14	0.19	18.74	59.74	-	1.20	-	-
CC-4b-2	8.03	8.59	3.37	0.24	0.94	0.12	0.14	18.88	59.69	0.40	1.26	3.06	-
CC-4b-3	7.61	8.50	3.35	0.25	1.31	0.14	0.16	18.89	59.79	-	1.22	2.52	-
CC-4b-4	7.61	8.73	3.35	0.20	1.16	0.14	0.15	18.90	59.76	0.38	1.41	3.52	-
CC-4b-5	7.61	8.73	3.35	0.20	1.16	0.14	0.15	18.90	59.76	-	1.21	3.15	-
CC-4c-1	7.94	8.58	3.28	0.28	0.93	0.13	0.12	19.02	59.73	-	1.04	-	-
CC-4c-2	7.70	8.64	3.32	0.25	0.94	0.13	0.15	19.09	59.79	-	1.03	3.16	-
CC-4c-3	7.45	8.99	3.34	0.22	0.83	0.15	0.11	19.14	59.78	0.42	1.33	3.43	-
CC-4c-4	7.91	8.46	3.21	0.23	1.27	0.12	0.20	18.83	59.77	0.41	1.61	4.28	-
CC-4c-5	8.10	8.66	3.06	0.23	1.05	0.11	0.16	18.90	59.73	0.49	1.67	4.36	-
CC-5c-1	7.93	8.59	3.17	0.21	1.24	0.11	0.17	18.82	59.75	0.39	1.35	3.58	-
CC-5c-2	8.00	8.29	3.26	0.25	1.34	0.12	0.18	18.80	59.76	0.38	1.39	3.65	-
RCa-1a-1	7.95	8.26	3.42	0.29	1.28	0.12	0.16	18.79	59.72	0.89	1.56	4.77	-

Table 3 (cont'd).

Sample	Ca	Mg	Fe	Na	Al	Mn	Ti	Si	O	(*) ppm La*	Ce*	Nd*	Sm*
RCa-1a-2	8.21	8.18	2.93	0.27	1.87	0.10	0.20	18.49	59.75	0.45	1.41	3.85	1.66
RCa-1a-3	8.17	8.37	2.91	0.24	1.48	0.10	0.17	18.78	59.79	0.29	0.93	2.49	1.16
RCa-1a-4	7.85	8.55	3.16	0.25	1.38	0.14	0.20	18.73	59.75	0.26	0.89	2.26	0.86
RCa-1a-5	8.22	8.54	2.88	0.25	1.18	0.13	0.14	18.92	59.76	0.37	1.63	3.63	1.59
RCa-1a-6	8.07	8.58	2.88	0.24	1.23	0.12	0.13	18.97	59.80	0.28	1.21	2.72	-
RCa-1b-1	8.17	8.39	2.92	0.27	1.59	0.09	0.18	18.65	59.74	0.41	1.59	3.97	-
RCa-1b-2	8.17	8.39	2.92	0.27	1.59	0.09	0.18	18.65	59.74	0.27	0.85	2.31	1.07
RCa-1b-3	7.89	8.74	2.88	0.27	1.38	0.10	0.14	18.84	59.77	-	0.81	1.74	-
RCa-1b-4	7.93	8.33	2.82	0.25	1.83	0.09	0.13	18.76	59.84	0.52	1.10	2.61	-
RCa-1b-5	8.00	8.82	2.84	0.24	1.13	0.11	0.14	18.96	59.77	0.18	0.73	1.70	-
RCa-2a-2-1	7.93	8.79	3.03	0.18	1.06	0.13	0.14	18.98	59.78	0.75	1.44	3.43	-
RCa-2a-2-2	7.74	8.49	3.17	0.23	1.41	0.12	0.15	18.88	59.81	-	1.08	-	-
RCa-2a-3-1	8.02	8.40	3.21	0.25	1.27	0.11	0.15	18.84	59.75	-	1.07	2.37	-
RCa-2a-4-1	8.03	8.47	3.20	0.25	1.16	0.11	0.13	18.90	59.75	-	-	-	-
RCa-2a-4-2	7.59	8.67	3.05	0.25	1.05	0.12	0.12	19.25	59.89	-	0.91	2.78	-
RCa-2a-6-1	7.91	8.10	3.27	0.27	1.46	0.10	0.14	18.92	59.83	-	1.15	3.16	-
RCa-3-1	7.62	8.51	3.42	0.24	1.52	0.14	0.17	18.64	59.73	-	1.18	3.33	-
RCa-3-2	7.20	8.84	3.52	0.23	0.94	0.15	0.14	19.16	59.83	-	1.20	2.77	-
RCa-3-3	7.63	8.84	3.29	0.21	0.89	0.12	0.14	19.10	59.79	-	1.10	3.14	-
RCa-3-4	7.61	8.74	3.38	0.24	1.11	0.13	0.15	18.90	59.74	-	1.05	3.49	-
RCa-3-5	7.94	8.50	3.17	0.26	1.20	0.12	0.13	18.92	59.76	0.35	1.02	2.40	-

Table 3 (cont'd).

										(*) ppm			
Sample	**Ca**	**Mg**	**Fe**	**Na**	**Al**	**Mn**	**Ti**	**Si**	**O**	**La***	**Ce***	**Nd***	**Sm***
RCa-3-6	8.02	8.54	3.16	0.24	1.12	0.11	0.15	18.91	59.75	0.29	0.96	2.30	-
RCa-3-7	7.85	8.50	3.27	0.22	1.36	0.13	0.18	18.74	59.75	0.35	1.47	2.97	-
RCa-3-8	7.99	8.33	3.29	0.24	1.33	0.12	0.18	18.77	59.75	0.34	1.64	3.63	1.43
RCa-3-ecu1	7.23	9.14	3.47	0.18	0.70	0.16	0.12	19.20	59.79	0.51	1.18	2.52	-
RCa-3-ecu	7.16	8.76	3.37	0.19	1.04	0.16	0.12	19.28	59.91	-	0.89	2.04	-

Table 3 (cont'd).

ENSTATITE GEOCHEMICAL DATA

Sample	Na	Mg	Al	Si	Ca	Ti	Mn	Fe	O
CC 1b-1	0.02	13.73	0.58	19.32	0.76	0.10	0.18	5.47	59.85
CC 1b-2	0.02	13.36	0.88	19.24	0.74	0.08	0.18	5.64	59.87
CC 1b-3	0.01	13.90	0.87	19.09	0.72	0.07	0.19	5.34	59.80
CC 1b-4	0.02	14.20	0.36	19.51	0.64	0.04	0.18	5.17	59.86
CC 5a-1	0.01	14.07	0.68	19.14	0.69	0.08	0.19	5.37	59.78
CC 5a-2	0.01	13.98	0.65	19.21	0.63	0.07	0.18	5.47	59.80
CC 5a-3	0.01	14.10	0.65	19.20	0.64	0.08	0.17	5.34	59.80
CC 5a-4	0.02	13.77	0.94	19.13	0.72	0.08	0.18	5.34	59.84
CC 5a-5	0.02	13.77	0.97	19.12	0.69	0.07	0.18	5.35	59.83
CC 5a-6	0.02	13.76	0.96	19.04	0.70	0.07	0.17	5.50	59.79
CC 5a-7	0.01	13.83	0.95	19.07	0.70	0.08	0.18	5.36	59.81
CC 5b-1	0.03	13.89	0.99	19.07	0.64	0.07	0.17	5.34	59.81
CC 5b-2	0.01	14.24	1.00	19.03	0.55	0.07	0.15	5.16	59.80
CC 5b-3	0.02	14.23	1.09	18.91	0.58	0.07	0.16	5.19	59.76
CC 5b-4	0.01	14.13	1.14	18.99	0.61	0.08	0.14	5.10	59.82
CC 5b-5	0.01	14.53	0.73	19.29	0.56	0.05	0.12	4.88	59.85
CC 5b-6	0.03	14.33	0.72	19.35	0.57	0.05	0.14	4.95	59.87
CC 5b-7	0.02	14.21	1.08	19.05	0.54	0.07	0.13	5.08	59.82
CC 6a-1	0.02	13.66	0.83	19.10	0.80	0.10	0.20	5.50	59.80
CC 6a-2	0.03	14.05	1.32	18.56	0.75	0.08	0.18	5.39	59.65
CC 6a-3	0.02	13.06	1.44	18.98	0.74	0.09	0.18	5.60	59.89
CC 6a-4	0.02	13.69	0.45	19.47	0.75	0.07	0.21	5.46	59.88
CC 6b-2-1	0.01	13.81	0.53	19.36	0.67	0.06	0.17	5.54	59.84
CC 6b-2-2	0.02	13.70	0.79	19.15	0.81	0.10	0.18	5.44	59.81
CC 6b-2-3	0.02	13.66	0.67	19.33	0.74	0.08	0.19	5.45	59.87
CC 6b-2-4	0.01	13.79	0.82	19.15	0.67	0.09	0.18	5.48	59.82
CC 6b-2-5	0.03	13.51	0.86	19.12	0.71	0.07	0.21	5.69	59.81
RCa 2a-1-1	0.01	13.66	0.60	19.34	0.71	0.06	0.17	5.59	59.85
RCa 2a-1-2	0.01	13.68	0.64	19.31	0.67	0.07	0.18	5.58	59.85
RCa 2a-1-3	0.01	13.88	0.46	19.37	0.69	0.07	0.18	5.52	59.83
RCa 2a-1-4	0.02	13.88	0.59	19.26	0.67	0.08	0.20	5.49	59.81
RCa 4-1	0.01	13.78	0.47	19.43	0.74	0.06	0.18	5.48	59.86
RCa 4-2	0.01	13.85	0.55	19.35	0.69	0.07	0.18	5.45	59.85
RCa 4-3	0.01	13.98	0.35	19.49	0.71	0.07	0.19	5.35	59.86

Table 4. Major element data of enstatite from corestone system 0512008.

Sample	Na	Mg	Al	Si	Ca	Ti	Mn	Fe	O
RCa 4-4	0.01	13.76	0.54	19.40	0.65	0.07	0.17	5.55	59.86
RCa 4-5	0.01	13.73	0.71	19.23	0.73	0.08	0.17	5.50	59.83
RCa 4-6	0.02	13.73	0.74	19.22	0.70	0.09	0.20	5.48	59.83
RCa 6b-1	0.02	13.78	0.67	19.23	0.71	0.09	0.19	5.49	59.83
RCa 6b-2	0.01	13.92	0.49	19.45	0.70	0.05	0.19	5.32	59.87
RCa 6b-3	0.01	14.04	0.38	19.51	0.68	0.05	0.18	5.29	59.87
RCa 6b-4	0.02	13.99	0.33	19.54	0.70	0.06	0.18	5.31	59.88

Table 4 (cont'd).

REFERENCES

REFERENCES

Banfield, J.F., and Eggleton, R.A., 1989. Apatite replacement and rare earth mobilization, fractionation, and fixation during weathering: Clays Clay Mineralogy, 37, 113–127.

Brantley, S.L. and Chen, Y., 1995. Chemical Weathering Rates of Pyroxenes and Amphiboles: Reviews in Mineralogy, 31, 119-172.

Cameron, B.I., 1998. *Melt generation and magma evolution in southeastern Guatemala.* Dissertation, Northern Illinois University, 400 p.

Cameron, B.I.B, Walker, J.A., Carr, M.J., Patino, L.C., Matiás, O., Feigenson, M.D., 2003. Flux versus decompression melting at stratovolcanoes in southeastern Guatemala: Journal of Volcanology and Geothermal Research, 119, 21-50.

Cameron, M., and Papike, J.J., 1981. Structural and chemical variations in pyroxenes: American Mineralogist, 66, 1-50.

Carr, M.J., Feigenson, M.D., Patino, L.C. and Walker, J.A. 2003. *Inside the Subduction Factory*, Geophysical Monograph v. 138; p. 153-179.

Carson, M.A., and Kirkby, M.J., 1972. *Hillslope Form and Process.* Cambridge University Press, Cambridge, UK.

Cotten, J., Le Dez, A., Bau, M., Caroff, M., Maury, R.C., Dulski, P., Fourcade, S., Bohn,M., Brousse, R., 1995. Origin of anomalous rare-earth element and yttrium enrichments in subaerially exposed basalts: evidence from French Polynesia: Chemical Geology, 119, 115–138.

Deer, W.A., Howie, R.A., Zussman, J., 1992. *An introduction to the rock-forming minerals.* Pearson Education Limited, Essex, London, 695.

Eggleton, R.A., Foudoulis, C., and Varkevisser, D., 1987. Weathering of basalt: Changes in rock chemistry and mineralogy: Clays and Clay Minerals, 35, 161-169.

Elderfield, H., Upstill-Goddard, R., and Sholkovitz, E.R., 1990. The rare earth elements in rivers, estuaries, and coastal seas and their significance to the composition of ocean waters: Geochimica et Cosmochimica Acta, 54, 971-991.

Fodor, R.V., Frey, F.A., Bauer, G.R. and Clague, D.A., 1992. Ages, rare-earth element enrichment, and petrogenesis of tholeiitic and alkalic basalts from Kahoolawe Island, Hawaii: Contributions to Mineralogy and Petrology, 110, 442-462.

Hanson, G.N., 1989. An approach to trace element modeling using a simple igneous systems as an example. Pp. 79-97 in: *Geochemistry and Mineralogy of Rare*

Earth Elements (B.R. Lipin and G.A. McKay, editors). Reviews in Mineralogy, 2I, Mineralogical Society of America, Washington, D.C.

Harlavan, Y., and Erel, Y., 2002. The release of Pb and REE from granitoids by the dissolution of accessory phases: Geochimica et Cosmochimica Acta, 66, 837-848.

Hochella, M.F., Jr., and Banfield, J.F., 1995. Chemical weathering of silicates in nature: A microscopic perspective with theoretical considerations. Pp. 353-406 in: *Chemical Weathering Rates of Silicate Minerals* (A.F. White and S.L. Brantley, editors). Reviews in Mineralogy, 31, Mineralogical Society of America, Washington, D.C.

James, O.B., Floss, C., and McGee, J.J., 2002. Rare earth element variations resulting from inversion of pigeonite and subsolidus reequilibration in lunar ferroan anorthosites: Geochimica et Cosmochimica Acta, 65, 1269-1284.

Johnsson, M.J., 1993. Chemical weathering controls on sand composition: Encyclopedia of Earth System Science, 1, 455-466.

Kushel, E. and Smith, I.E.M., 1992. Rare earth mobility in young arc-type volcanic rocks from northern New Zealand: Geochimica et Cosmochimica Acta, 56: 395 l-3955.

McKay, G.A., 1989. Partitioning of rare earth elemnts between major silicate minerals and baslatic melts: Reviews in Mineralogy, 21, 45-77.

Minarik, L., Zigova, A., Bendl, J., Skrivan, P., and Stastny, M., 1998. The behaviour of rare-earth elements and Y during the rock weathering and soil formation in the Ricany granite massif, Central Bohemia, The Science of the Total Environment, 215, 101-111.

Mitchell, T.D., Hulme, M., and New, M., 2002. Climate data for political areas: Center for Climate Change, Area 34: 109-112.

Morimoto, N., Fabries, J., Ferguson, A.K., Ginzburg, I.V., Ross, M., Seifert, F.A., Zussman, J., Aoki, K., and Gottardi, G., 1988. Nomenclature of pyroxenes: Mineralogical Magazine, 52, 535-550.

Nesbitt, H.W., and Young, G.M., 1982. Early Proterozoic climates and plate motions inferred from major element chemistry of lutites: Nature, 299, 715-717.

Nesbitt, H.W., 1979. Mobility and fractionation of rare earth elements during weathering of granodiorite: Nature, 279, 206-210.

Nesbitt, H.W., and Wilson, R.E., 1992. Recent chemical weathering of basalts: American Journal of Science, 292, 740-777.

Norman, M.D., Pearson, N.J., Sharma, A., and Griffin, W.L., 1996. Quantitative analysis of trace elements in geological materials by laser ablation ICPMS: instrumental

operating conditions and calibration values of NIST glasses: Geostandards Newsletter, 20, 247-261.

Ollier, C.D., 1971. Causes of spheroidal weathering: Earth-Science Reviews, 7, 127-141.

Onuma, N., Higuchi, H., Wakita, H., and Nagasawa, H.,1968. Trace element partition between two pyroxenes and the host lava: Earth and Planetary Science Letters, 5, 47-51.

Patino, L.C., Velbel, M.A., Price, J.R., and Wade, J.A., 2003. Trace element mobility during spheroidal weathering of basalts and andesites in Hawaii and Guatemala: Chemical Geology, 202, 343– 364.

Price, J.R. and Velbel, M.A., 2003. Chemical weathering indices applied to weathering profiles developed on heterogeneous felsic metamorphic parent rocks: Chemical Geology, 202, 397-416.

Price, R.C., Gray, C.M., Wilson, R.E., Frey, F.A., and Taylor, S.R., 1991. The effects of weathering on rare-earth element, Y and Ba abundances in Tertiary basalts from southeastern Australia: Chemical Geology, 93, 245-265.

Reynolds, J.H., 1987. Timing and sources of Neogene and Quaternary volcanism in south-central Guatemala: Journal of Volcanology and Geothermal Research, 33, 9-22.

Roden, M.F., Frey, F.A. and Claguc, D.A., 1984. Geochemistry of tholeiitic and alkalic lavas from the Koolau Range, Oahu. Hawaii: implications for Hawaiian volcanism: Earth and Planetary Science Letters, 69: 141-158.

Sak, P.B., Fisher, D.M., Gardner, T.W., Murphy, K., Brantley, S.L., 2004. Rates of weathering rind formation on Costa Rican basalt: Geochimica et Cosmochimica Acta, 68, 1453-1472.

Stoops, G., Altemuller, H.J, Bisdom, F.B.A., Delvigne, J., Dobrovolsky, V.V., Fitzpatrick, E.A., Paneque, G. and Sleeman, J., 1979. Guidelines for the description of mineral alterations in soil micromorphology: Pedologie, 29, 121-135.

Taylor, G., and Eggleton, R.A., 2001. *Regolith Geology and Geomorphology.* John Wiley and Sons, Ltd, West Sussex, England.

Velbel, M.A., 1989. Weathering of hornblende to ferruginous products by a dissolution-reprecipitation mechanism: Petrography and stoichiometry. Clays and Clay Minerals, v. 37, p. 515-524.

Velbel, M.A., 2007. Surface textures and dissolution processes of heavy minerals in the sedimentary cycle: examples from pyroxenes and amphiboles: Pp. 113-150 in

Heavy Minerals in Use (M. Mange and D. Wright, editors). Developments in Sedimentology, 58, Elsevier, Amsterdam.

Velbel, M.A., and Barker, W.W., 2008. Pyroxene weathering to smectite: Conventional and low-voltage cryo-field emission scanning electron microscopy, Koua Bocca ultramafic complex, Ivory Coast. Clays and Clay Minerals, v. 56, p. 111-126.

Wade, J.A., 2002. *Element mobility and secondary mineral formation during the early stages of alteration in rocks from the Tecuamburro volcanic complex, Southeast Guatemala*: Master's Thesis, Michigan State University, 194.

Walker, J.A., Roggensack, K., Patino, L.C., Cameron, B.I., and Otoniel, M., 2003. The water and trace element contents of melt inclusions across an active subduction zone: Contrib. Mineral. Petrol., 146, 62–77.

White, A.F., and Brantley, S.L., eds, 1995. *Chemical Weathering Rates of Silicate Minerals*: Reviews in Mineralogy, 31, Mineralogical Society of America, Washington, D.C.

Wood, S.A., 1990. The aqueous geochemistry of the rare earth elements and yttrium: Chemical Geology, 82, 159-186.